Development of Geothermal Reservoir Simulator for Predicting Three-dimensional Water-Steam Flow Behavior Considering Non-equilibrium State and Kazemi/MINC Double Porosity System

Sumire Fujii, Yuki Ishigami and Masanori Kurihara

Waseda University

Keywords

Geothermal simulator, Kinetic non-equilibrium phase change, double porosity, MINC model, artificial recharge

ABSTRACT

Although the reservoir simulation is widely utilized to predict geothermal reservoir performances, the results of the simulation are sometimes different from those actually observed in field operations due to non-equilibrium conditions. For example, the recharge water sometimes reaches producing wells much earlier than predicted by reservoir simulation. Therefore, in this research, we attempted to develop a numerical simulator that can deal with the non-equilibrium vaporization of water and condensation of steam for predicting geothermal reservoir performances more accurately.

First, we developed a three-dimensional simulator that can predict the flow behavior of geothermal fluids in a non-equilibrium state. Conventional geothermal simulators solve the only material balance equation for all the water molecules regardless of the phase condition. On the other hand, in the simulator developed in this research, water molecules in the liquid phase are distinguished from those in vapor phase, and the two material balance equations are derived for water and steam separately. These equations have the terms to express the molecular transportation from steam to water and vice versa. Non-equilibrium vaporization and condensation of water molecules are expressed by adjusting the kinetic rate of transportation of water molecules across phases.

Next, we expanded the functions of the above simulator, incorporating two types of double porosity models, Kazemi and MINC, to reproduce the fluid flow preferentially through fractures and faults.

After verifying the simulator functions, we investigated how the speed of the transportation of water molecules across phases affected the geothermal reservoir performances, especially those with recharging water. Case studies revealed that the non-equilibrium condition hastened the movement of the water injected as recharge water through fractures, which

resulted in the water breakthrough earlier than predicted by conventional (equilibrium type) simulators.

1. Introduction

Geothermal power generation is one of the most promising renewable energies because it can steadily generate electricity for 24 hours without being affected by the weather. Reservoir simulation is widely utilized to predict the production of geothermal energy (i.e., steam and hot water). It is experienced, however, that the results of reservoir simulation are sometimes different from those actually observed in field operations due to the non-equilibrium state.

Artificial recharge is popularly used in geothermal power generation. This method is essential to enable the long-term production of steam by injecting water into a geothermal reservoir. However, the recharge water sometimes reaches producing wells earlier than predicted by reservoir simulation.

One of the reasons for this mis-prediction is the non-equilibrium effects. That is, the injected water does not easily vaporize even if the reservoir condition is in the steam region far from the water-steam equilibrium condition. Another reason is the presence of fractures. In the geothermal reservoir, there exist many fractures, which become the main paths of fluid flow. If fractures connect an injection well to a production well, the breakthrough of injected water at the production well will be significantly hastened.

Therefore, in this research, we attempted to develop a simulator that can deal with the non-equilibrium state and the fractured system to predict geothermal reservoir performances more accurately.

This simulator can deal with the non-equilibrium state, which will contribute to achieving more accurate predictions efficiently. In conventional reservoir simulation, it is assumed that phase change occurs in the equilibrium state. When solving equations in a simulator, the temperature within each grid is regarded as uniform. In reality, however, the temperature of the fluid and the rock should vary within each grid due to a temperature gradient. This is one of the reasons why the equilibrium state is not necessarily established. It is true that the equilibrium state can be expected if the grid size is sufficiently small, but such small grids are not assigned in usual simulation, taking the computational time into consideration. The simulator dealing with non-equilibrium state can enable the prediction of more accurate phase alteration in a reasonably short simulation time.

We developed the simulator from scratch and validated it using the commercial thermal simulator, STARS, developed by Computer Modelling Group Ltd. (CMG). Since the computational results of our simulator assuming the equilibrium state well matched those of STARS, we could confirm that our simulator can calculate reservoir behavior in the equilibrium state accurately. Next, in order to investigate the reservoir performances in the non-equilibrium state, we conducted the simulation specifying the smaller kinetic rate constant of "K_{gen}" (1E-8 1/s/K) than that for the equilibrium condition. The results showed that the water production started far earlier in the non-equilibrium state than in the equilibrium condition.

Finally, we added the two types of double porosity models (Kazemi and MINC), which are popularly used in geothermal reservoir simulation, into the simulator developed in the above.

The simulation using these fracture models suggested that the water flowed dominantly in fractures and that the effects of non-equilibrium state on the water flow is much more significant in fractures than in matrices, which induced the earlier breakthrough of water.

Through this research, we confirmed that we can predict more accurate geothermal reservoir performances by considering both the non-equilibrium state and the fracture system.

2. Reservoir Simulator (Single Porosity)

We developed a three-dimensional simulator that can predict the flow behavior of geothermal fluids in the non-equilibrium state.

2.1 Governing Equations

Conventional simulators usually solve mass balance equation and energy balance equation assuming the equilibrium state. On the other hand, in the simulator developed in this research, water molecules in the liquid phase are distinguished from those in vapor phase, and the material balance equations are derived for water and steam separately. These new material balance equations have the terms of n_s [mol/m^3/s] and n_w [mol/m^3/s], which express the rate of molecular transportation from water to steam and vice versa. The non-equilibrium vaporization and condensation of water molecules are expressed by adjusting the kinetic rates of the transportation of water molecules across the phases.

$$\vec{\nabla}\cdot\left(k\frac{k_{rw}\rho_w}{\mu_w}(\vec{\nabla}P-\overline{\rho}_w g\vec{\nabla}D)\right)+n_w-n_s+\tilde{q}_{w\_in}\rho_{w\_in}+\tilde{q}_{w\_out}\rho_{w\_out}=\frac{\partial}{\partial t}\left(\phi S_w\rho_w\right) \tag{1}$$

$$\vec{\nabla}\cdot\left(k\frac{k_{rs}\rho_s}{\mu_s}(\vec{\nabla}P-\overline{\rho}_s g\vec{\nabla}D)\right)-n_w+n_s+\tilde{q}_{s\_in}\rho_{s\_in}+\tilde{q}_{s\_out}\rho_{s\_out}=\frac{\partial}{\partial t}\left(\phi S_s\rho_s\right) \tag{2}$$

$$\begin{aligned}&\vec{\nabla}\cdot\left(k\frac{k_{rw}\rho_w H_w}{\mu_w}(\vec{\nabla}P-\overline{\rho}_w g\vec{\nabla}D)\right)+\vec{\nabla}\cdot\left(k\frac{k_{rs}\rho_s H_s}{\mu_s}(\vec{\nabla}P-\overline{\rho}_s g\vec{\nabla}D)\right)+\vec{\nabla}\cdot\left(\lambda_{all}\vec{\nabla}\cdot T\right)\\&+\tilde{q}_{w\_in}\rho_{w\_in}H_{w\_in}+\tilde{q}_{s\_in}\rho_{s\_in}H_{s\_in}+\tilde{q}_{w\_out}\rho_{w\_out}H_{w\_out}+\tilde{q}_{s\_out}\rho_{s\_out}H_{s\_out}\\&=\frac{\partial}{\partial t}\left(\phi S_w\rho_w U_w+\phi S_s\rho_s U_s+(1-\phi)\rho_r R_{capa}T\right)\end{aligned} \tag{3}$$

, where

- P: pressure [Pa]
- S_l: saturation of phase l
- k: absolute permeability [m^2]
- k_{rl}: relative permeability of phase l [-]
- ρ_l: molar density of phase l [mol/m^3]
- g: gravitational acceleration [m/s^2]
- D: depth [m]
- $q_{l\_in/out}$: injection/production rate of phase l per unit bulk volume [1/s]
- ϕ: porosity [-]
- H_l: molar enthalpy of phase l [J/mol]
- Ul: molar internal energy of phase l [J/mol]
- R_{capa}: specific heat of rock [J/mol/K]
- λ_{all}: overall thermal conductivity [J/s/m/K]
- T: temperature [K]

Our simulator solves Equations (1) through (3) for the three primary unknowns of pressure, temperature and water saturation. Since it is impossible to analytically solve the above system of non-linear partial differential equations, this equation system is discretized by the finite difference method and transformed into a non-linear equation system. This non-linear equation system then can be solved by the Newton-Raphson method that is one of the most popular numerical methods for solving a non-linear equation system.

2.2 Definition of n_s and n_w

The rates of molecular transportation n_s and n_w are evaluated based on the difference between reservoir temperature and water-steam equilibrium temperature, and on the kinetic rate constants of K_{gen_s} and K_{gen_w} for water and steam generation. Equation (4) expresses that water is generated when the grid temperature (T) is lower than the vaporization temperature (T_{vap}). Furthermore, Equation (4) expresses that water is produced more rapidly when the difference between the grid temperature and vaporization temperature becomes large. $\phi\rho_s S_s$ indicates the molar density of steam in each grid, and the larger this value becomes, the more water is likely to be generated. Steam generation term is likewise expressed as Equation (5). The equilibrium state can be reproduced with the large enough K_{gen_s} and K_{gen_w}, while the non-equilibrium state is expressed with the relatively small values of them.

$$n_w = \begin{cases} 0 & (T - T_{vap}) > 0 \\ K_{gen\_w}\,\phi S_s \rho_s (T_{vap} - T) & (T - T_{vap}) < 0 \end{cases} \tag{4}$$

$$n_s = \begin{cases} K_{gen\_s}\,\phi S_w \rho_w (T - T_{vap}) & (T - T_{vap}) > 0 \\ 0 & (T - T_{vap}) < 0 \end{cases} \tag{5}$$

The concept of molecular transportation rates of n_s and n_w is explained as follows:

For example, when water is injected into a steam-saturated grid, if injected water volume is small, the pressure-temperature condition of this grid may be still in the steam region as shown in the following P-T diagram (Figure 1). The pressure-temperature condition becomes closer to the vaporization line as the volume of injected water becomes larger.

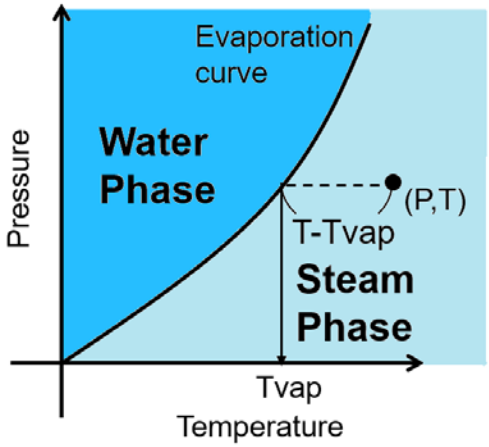

Figure 1: Relationship between T and Tvap expressed in P-T diagram

In conventional simulators, if the resultant pressure-temperature condition is in the steam region, all the water molecules are considered to be the steam state instantaneously conforming to the equilibrium condition. In our simulator, however, water molecules are considered to become the steam state gradually, depending on the kinetic rate constant, and on the product of $\phi\rho_w S_w$ and the deviation of pressure-temperature condition of a grid from the vaporization line as a driving force.

3. Validation

After constructing this new simulator, we confirmed that this simulator worked properly. The thermal simulator (STARS) developed by CMG was used for the validation of this simulator.

3.1 One-dimensional Model (Single Porosity)

To validate our simulator for the calculation of one-dimensional single porosity system, we conducted the simulation for the following three cases.

Case1: ”STARS”
The results calculated by STARS

Case2: ”FUJII K=1E-5”
The results calculated by our simulator assuming the equilibrium state with
$K_{gen\_s}=K_{gen\_w}$=1E-5 [1/s/K]

Case3: ”FUJII K=1E-8”
The results calculated by our simulator assuming the non-equilibrium state with
$K_{gen\_s}=K_{gen\_w}$=1E-8 [1/s/K]

Since STARS can deal with the equilibrium state only, the results of ”FUJII K=1E-5” (case2) should be in a good agreement with those of “STARS” (case1). ”FUJII K=1E-8” (case3) is expected to have different results from ”FUJII K=1E-5” (case2) and “STARS” (case1) because it calculates reservoir performances in the non-equilibrium state.

3.1.1 Simulation Specifications (Single Porosity)

As shown in Figure 2, the reservoir model used in all of the above three cases had dimensions of x=1000 [ft], y=100 [ft] and z=100 [ft] with 10*1*1 grid system. It was initially filled with steam of 1500 [psia] and 320 [K]. An injection well and a production well were located at grids (1,1,1) and (10,1,1), respectively. The injection rate was assumed to be 800 [ft^3/day] and the production rate was 800 [ft^3/day]. Injected water temperature was 50 [°C]. The other simulation specifications are shown in Table 1 and Figure 3.

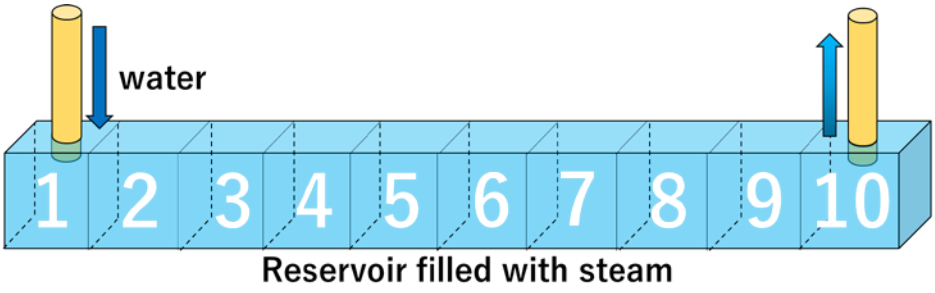

Figure 2: Reservoir model. Water is injected from grid 1 and fluid is produced from grid 10.

Table 1 Simulation specifications

Items	Description
Absolute permeability [mD]	100
Porosity at reference pressure ϕ_0 [-]	0.2
Compressibility of rock C_r [1/Pa]	1.4504×10^{-9}
Reference pressure P_{refp} [Pa]	101353.56
Rock heat capacity C_r [J/mol/K]	63.79
Density of rock ρ_r [mol/m^3]	38447.71
Time step [day]	1
Radius of injection well [inch]	6.0
Radius of production well [inch]	6.0

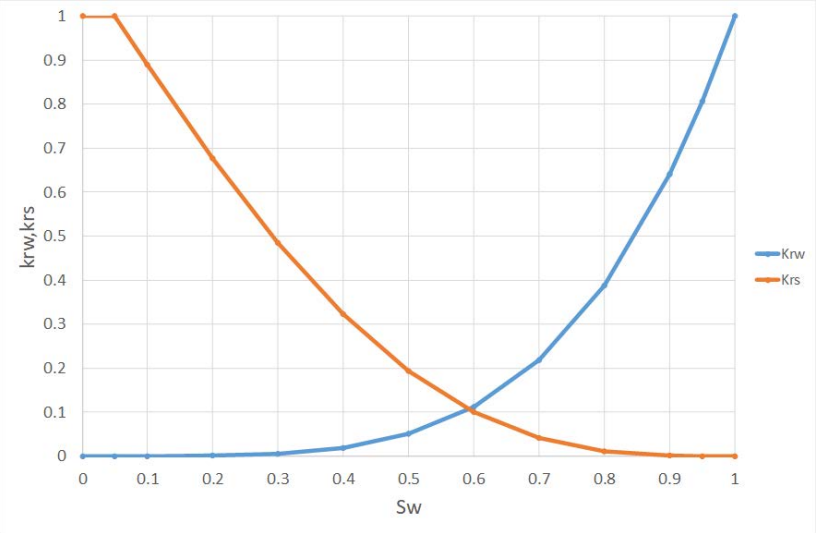

Figure 3: Relative permeability used in the simulation.

3.1.2 Validation and Case Study (Single Porosity)

First, we compared two cases of simulation, “STARS” (case1) and “FUJII K=1E-5” (case2). Since both of these cases assumed the equilibrium state, the results by our simulator agreed very well with those of STARS as shown in Figure 4 through Figure 6, which suggests the accuracy of our simulator.

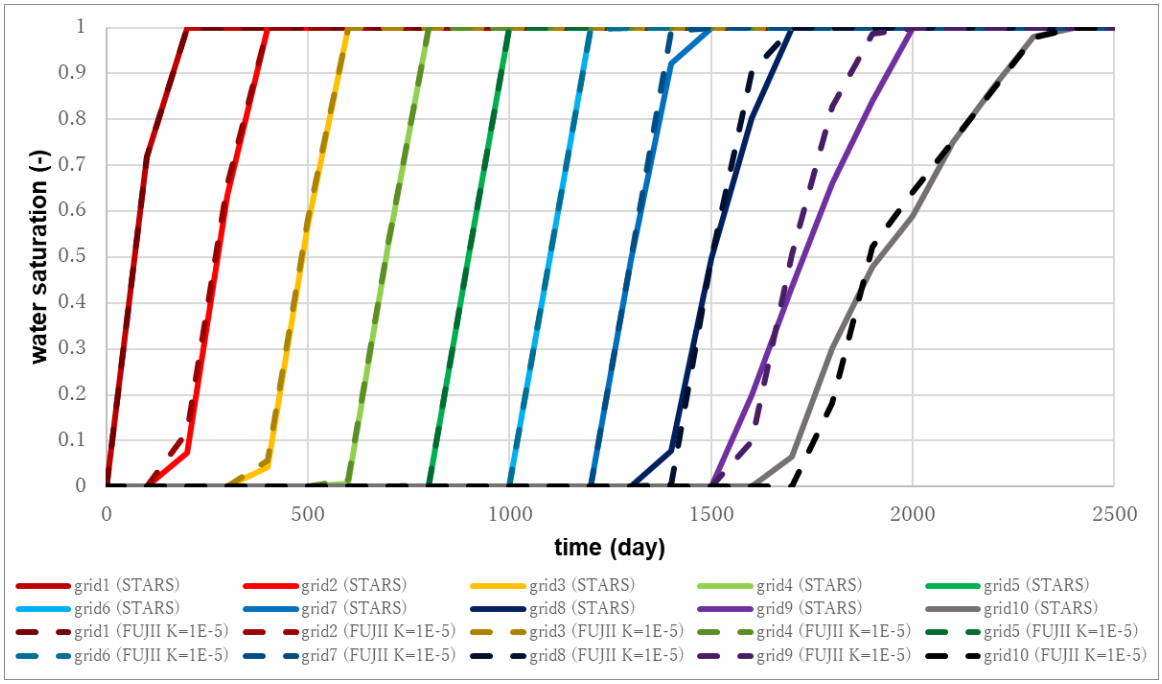

Figure 4: Time vs. Water saturation ("STARS"(case1) : equilibrium, "FUJII K=1E-5"(case2): equilibrium).

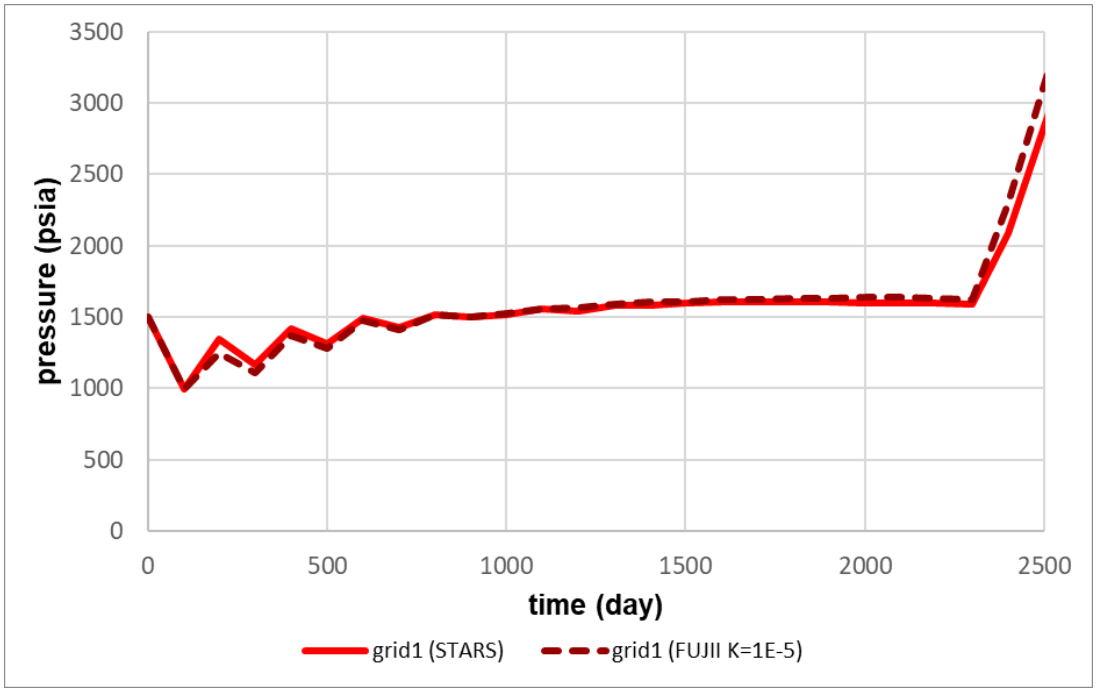

Figure 5: Time vs. Pressure ("STARS"(case1) : equilibrium, "FUJII K=1E-5"(case2): equilibrium).

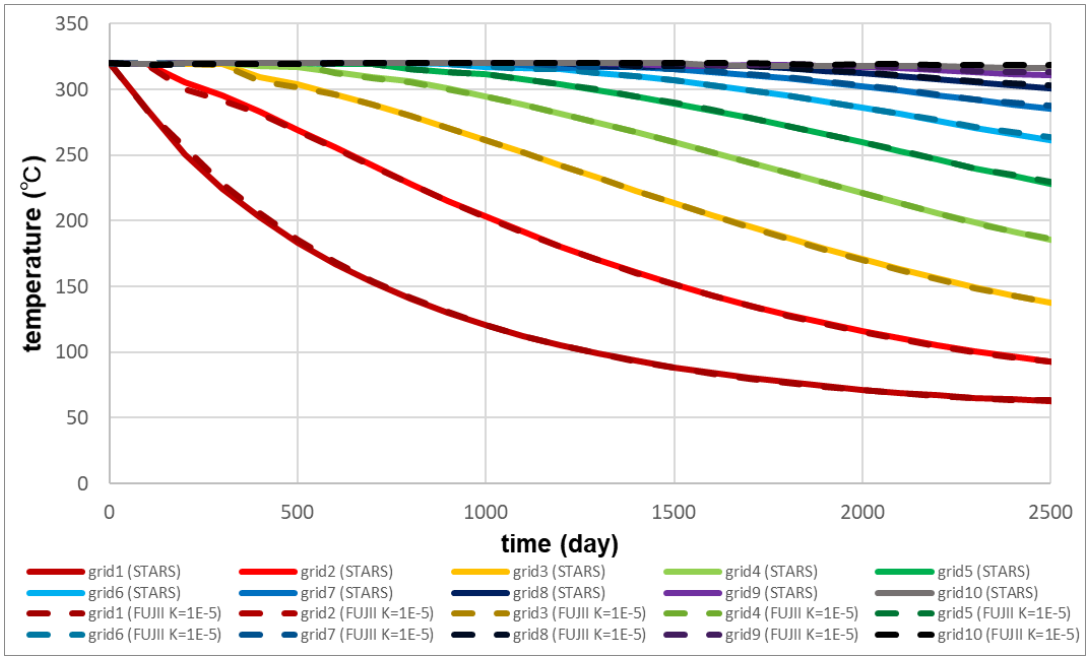

Figure 6: Time vs. Temperature ("STARS"(case1): equilibrium, "FUJII K=1E-5"(case2): equilibrium).

Next, we compared two cases of simulation, "STARS" (case1) and "FUJII K=1E-8" (case3). The results of "FUJII K=1E-8" (case3) shown in Figure 7 through Figure 9 were a little different from those of "STARS" (case1). Figure 7 shows that the water saturation started to increase earlier in "FUJII K=1E-8" (case3) than in "STARS" (case1), because in the non-equilibrium state, the injected water remained as water phase for a longer time than in the equilibrium state. Similarly, the timing when the water saturation reached 1 was retarded in "FUJII K=1E-8" (case3) in comparison with "STARS" (case1). The steam initially existing in each grid remains as steam for a longer time due to the non-equilibrium state even after the pressure-temperature condition of each grid became in the water region by the continuous water injection, which resulted in the slow changes in water saturation in the non-equilibrium state.

Figure 8 shows that the pressure changed more gradually in "FUJII K=1E-8" (case3) than in "STARS" (case1). In "STARS" (case1), pressure rapidly decreased when the phase altered from steam to water. In "FUJII K=1E-8" (case3), however, no abrupt pressure drop were observed because phase change occurred slowly in all the grids.

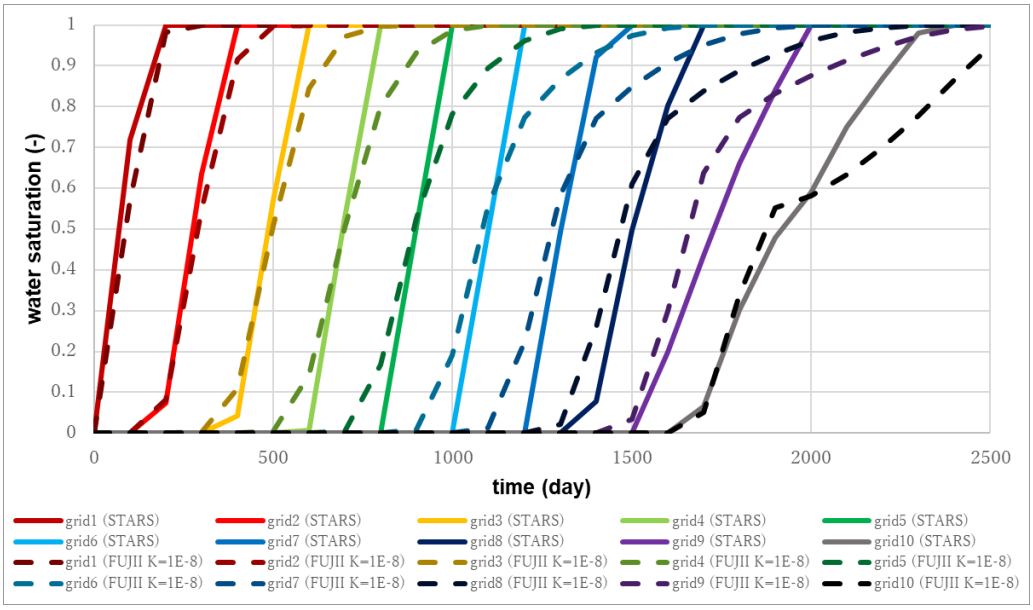

Figure 7: Time vs. Water saturation ("STARS"(case1): equilibrium, "FUJII K=1E-8"(case3): non-equilibrium).

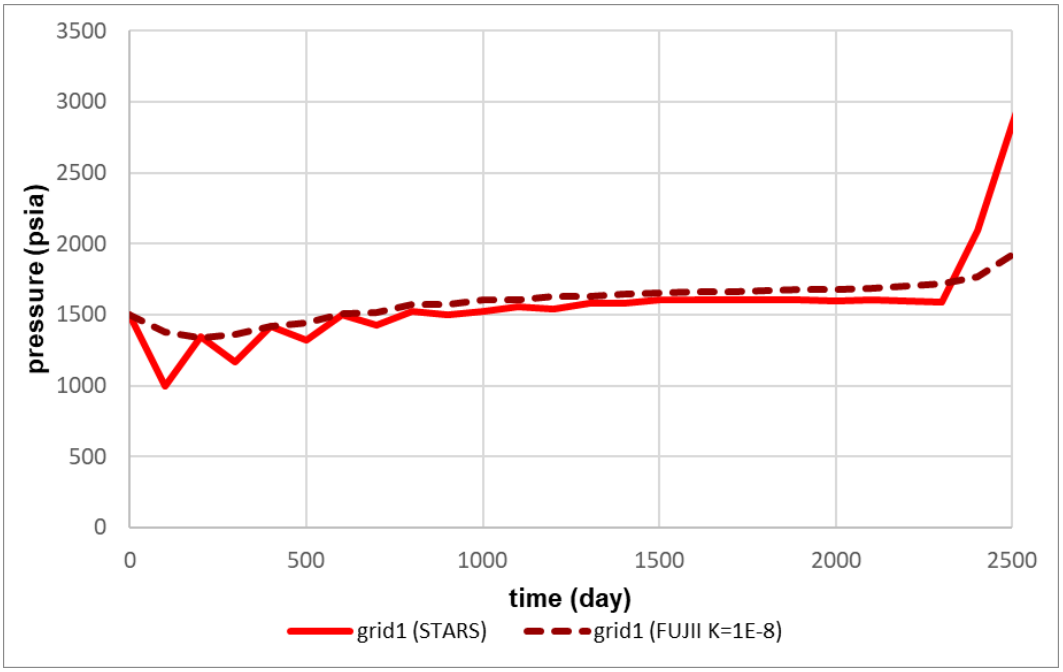

Figure 8: Time vs. Pressure ("STARS"(case1): equilibrium, "FUJII K=1E-8"(case3): non-equilibrium).

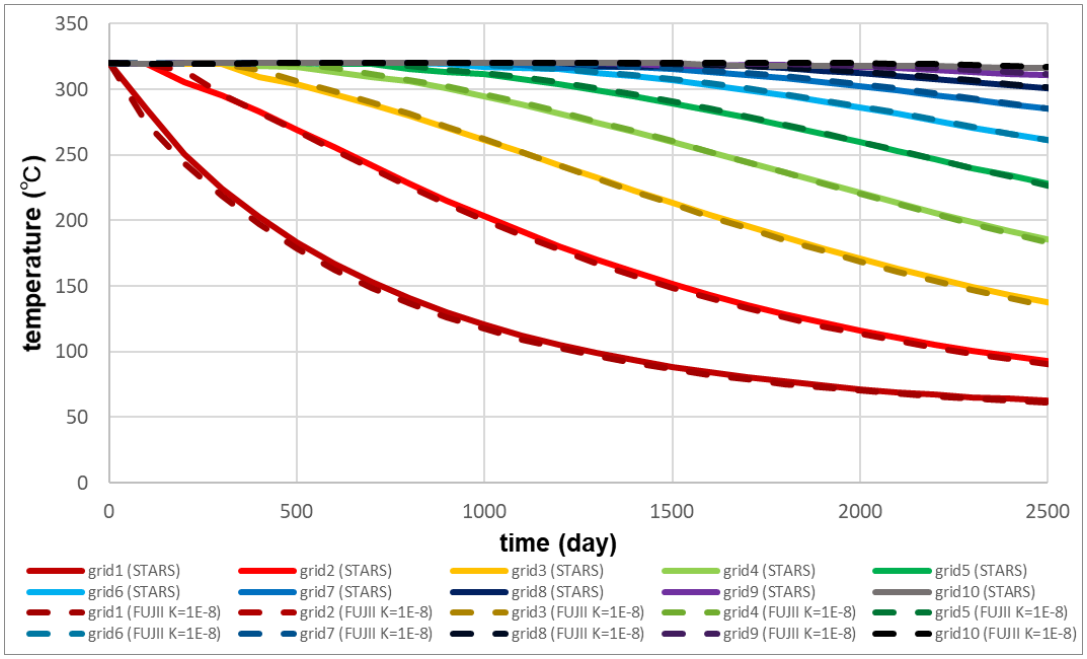

Figure 9: Time vs. Temperature ("STARS"(case1): equilibrium, "FUJII K=1E-8"(case3): non-equilibrium).

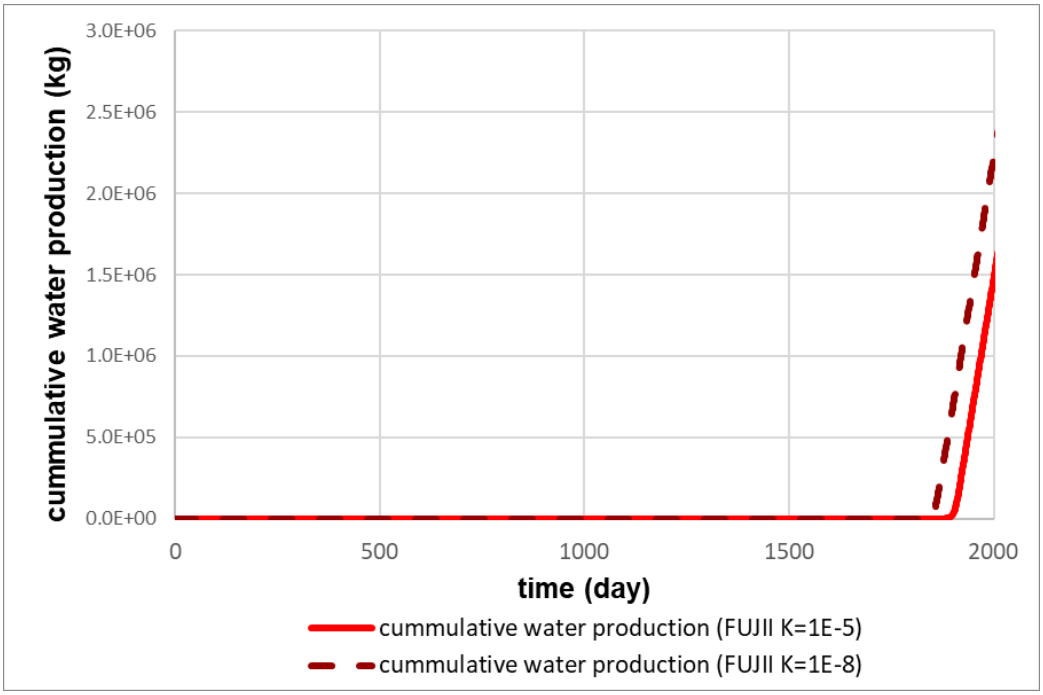

Figure 10: Cumulative water production ("FUJII K=1E-5"(case2): equilibrium, "FUJII K=1E-8"(case3): non-equilibrium).

Figure 10 shows that the production of water started earlier in non-equilibrium state. This is because water saturation starts to increase earlier in non-equilibrium state. Figure 11 shows the pressure and temperature traverse in the P-T diagram calculated by STARS and our simulator. In the cases assuming the equilibrium state (cases1 and 2), when the phase was altered from steam to water (in other words, when steam and water coexisted), the pressure and temperature changed along the vaporization line. On the other hand, pressure-temperature condition changed across the vaporization line in the non-equilibrium state (case3), even in the two-phase condition.

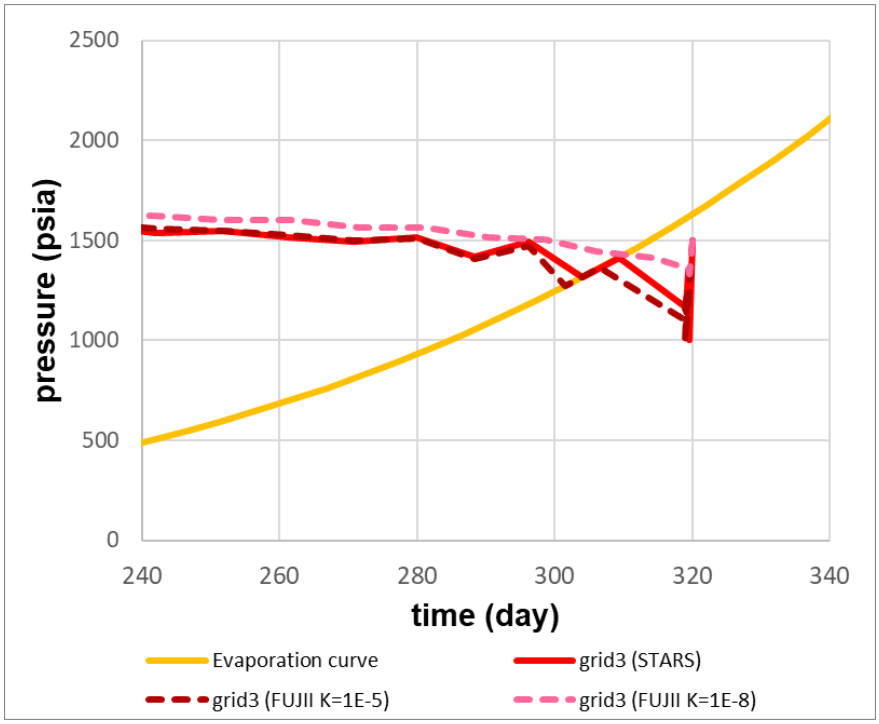

Figure 11: Temperature vs. Pressure (“STARS”(case1), “FUJII K=1E-5”(case2): equilibrium, “FUJII K=1E-8”(case3): non-equilibrium).

3.2 Three-dimensional Model (Single Porosity)

Similarly, we validated our simulator for the three-dimensional single porosity system. We conducted the simulation for the following three cases.

Case1: ”STARS”
The results calculated by STARS

Case2: ”FUJII K=1E-5”
The results calculated by our simulator assuming the equilibrium state with
$K_{gen\_s}=K_{gen\_w}$=1E-5 [1/s/K]

Case3: ”FUJII K=1E-8”
The results calculated by our simulator assuming the non-equilibrium state with
$K_{gen\_s}=K_{gen\_w}$=1E-8 [1/s/K]

3.2.1 Simulation Specifications (Single Porosity)

The reservoir model used in all of the above three cases had dimensions of x=600 [ft], y=600 [ft] and z=600 [ft] with 3*3*3 grid system. It was initially filled with steam of 1300 [psia] and 320 [K]. An injection well and a production well were located at grids (1,1,3) and (3,3,3), respectively. The injection rate was assumed to be 1500 (ft^3/day) and the bottom hole pressure of production well was 1000 [psia]. Injected water temperature was 50 [℃]. The other simulation specifications are shown in Table 1 and Figure 3.

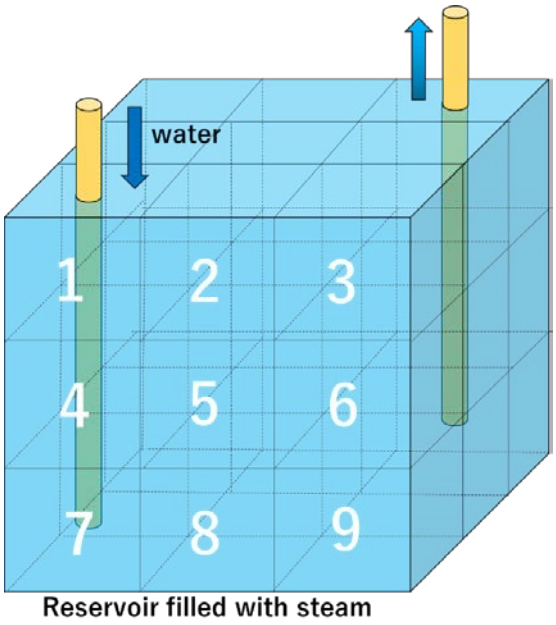

Figure 12: Reservoir model. Water is injected from grid 7 and fluid is produced from grid 27.

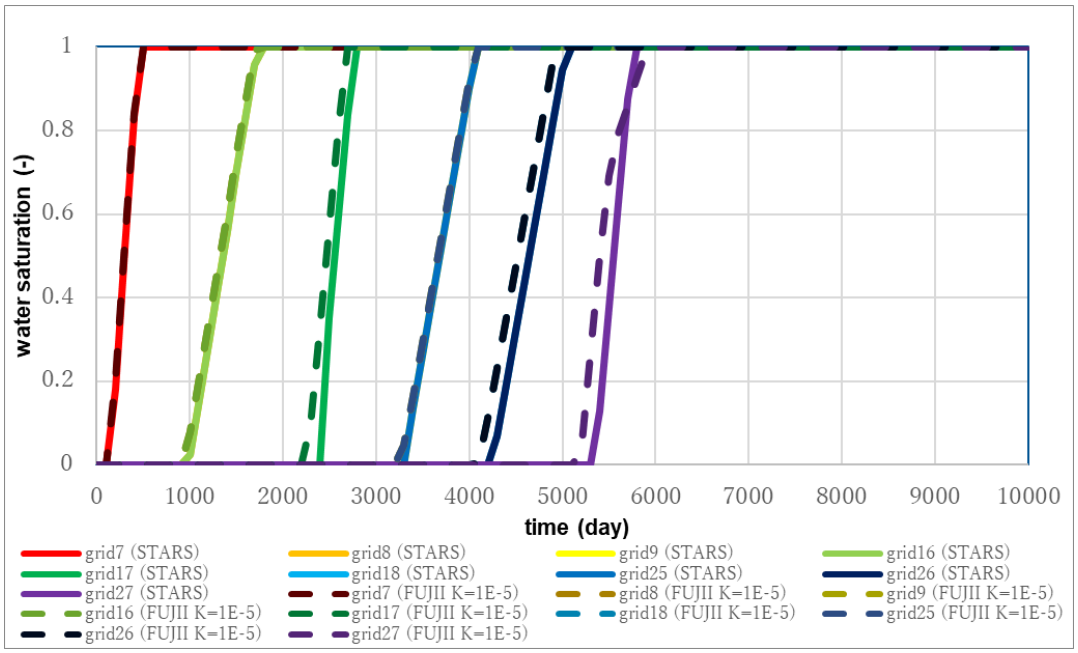

Figure 13: Time vs. Water saturation ("STARS"(case1): equilibrium, "FUJII K=1E-5"(case2): equilibrium).

3.2.2 Validation and Case Study (Single Porosity)

First, we compared two cases of simulation, “STARS” (case1) and “FUJII K=1E-5” (case2).

Since both of these cases assumed the equilibrium state, the results by our simulator agreed very well with those of STARS as shown in Figure 13 エラー! 参照元が見つかりません。, which suggests the accuracy of our simulator, as in the previous section.

Next, we compared two cases of simulation, “STARS” (case1) and “FUJII K=1E-8” (case3).

Even in the three-dimensional cases, the reservoir performances assuming the non-equilibrium state showed the tendencies similar to those in one-dimensional cases as depicted in Figure 14. Therefore, we conclude that we could successfully expand our simulator to three-dimensional system.

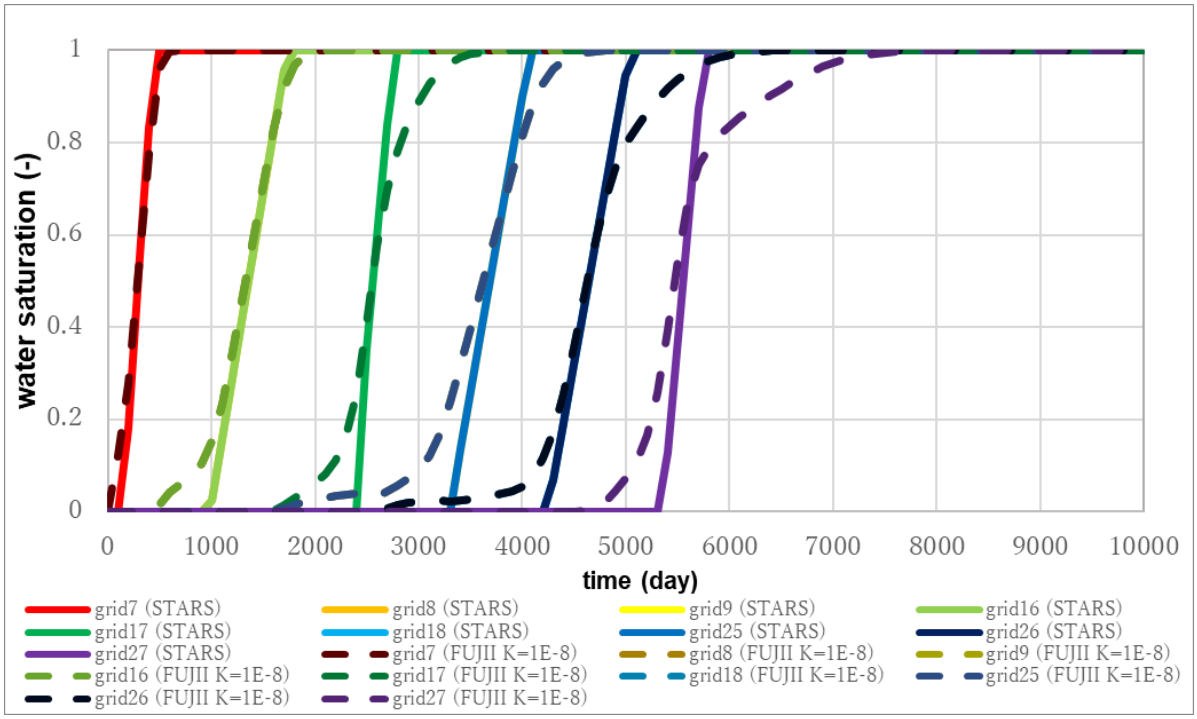

Figure 14: Time vs. Water saturation (“STARS”(case1): equilibrium, “FUJII K=1E-8”(case3): non-equilibrium).

3.3 Comparison with Small Grid Model (Single Porosity)

Aiming at examining how our simulator’s functions of calculation for the non-equilibrium state worked, we compared the results assuming the non-equilibrium state with those using the reservoir model composed of smaller grids through the following three cases.

Case1: “FUJII eq small”
The results calculated by our simulator using the model composed of smaller grids shown in the right side of Figure 15, assuming the equilibrium state with $K_{gen\_s}=K_{gen\_w}$=1E-5 [1/s/K]

Case2: “FUJII eq large”
The results calculated by our simulator using the model composed of large grids shown in the left side of Figure 15, assuming the equilibrium state with $K_{gen\_s}=K_{gen\_w}$=1E-5 [1/s/K]

Case3: “FUJII non-eq large”
The results calculated by our simulator using the model composed of large grids shown in the left side of Figure 15, assuming the non-equilibrium state with the following kinetic rate constants:

$K_{gen\_s}(1,1,1)=K_{gen\_w}(1,1,1)$=1E-9 [1/s/K], $K_{gen\_s}(2,1,1)=K_{gen\_w}(2,1,1)$=5E-9 [1/s/K],
$K_{gen\_s}(3,1,1)=K_{gen\_w}(3,1,1)$=1E-8 [1/s/K], $K_{gen\_s}(4,1,1)=K_{gen\_w}(4,1,1)$=5E-9 [1/s/K],
$K_{gen\_s}(5,1,1)=K_{gen\_w}(5,1,1)$=1E-9 [1/s/K]

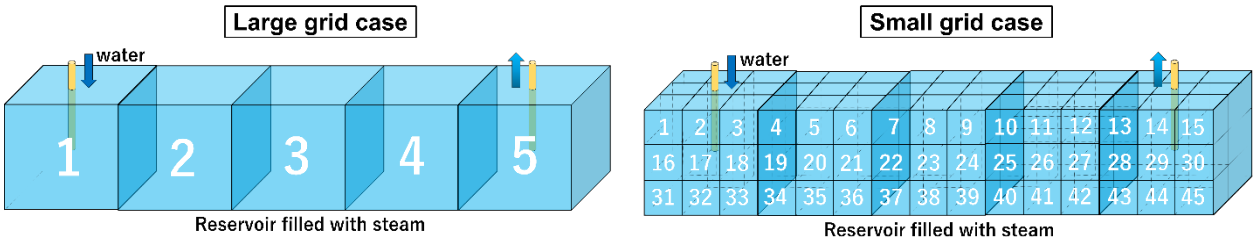

Figure 15: Grid system in the large grid case and the small grid case

It is expected that if the size of each grid is sufficiently small, the fluid flow in each grid can be accurately simulated even in assuming the equilibrium state. In this section, we examined how accurately “FUJII non-eq large” (case3) could calculate the reservoir performances by comparing its results with those of “FUJII eq small” (case1). Furthermore, if the results of case 3 is close enough to those of case 1, it is manifested that the non-equilibrium model can provide the results of the similar accuracy to fine grid model in much shorter computational time.

3.3.1 Simulation Specifications (Single Porosity)

The reservoir model used in this simulation had dimensions of x=1500 [ft], y=300 [ft] and z=300 [ft]. It was initially filled with steam of 1500 [psia] and 325 [K]. The injection rate was assumed to be 2000 [ft^3/day] and the bottom hole pressure of production well was assumed to be 1300 [psia]. Injected fluid temperature was 80 [°C]. The other properties are shown in Table 1 and Figure 3.

3.3.2 Case Study (Single Porosity)

We compared the results of the above three cases, which are depicted in Figure 20 through Figure 22. Figure 16 shows how water saturation changed in each case, where the water saturation of grid 1 in “FUJII eq small” (case1) denotes the average water saturation of all the small grids included in the large grid 1 (water saturations of grids 2-5 in “FUJII eq small” (case1) are defined similarly). Figure 20 through Figure 22 suggest that the results of “FUJII eq small” (case1) showed the tendencies similar to those of “FUJII non-eq large” (case3), (e.g., earlier start of increase in water saturation and slower speed of increase in water saturation). Although the results of case3 are somewhat different from those of case1, these differences should have been caused by the gravity effects and the insufficiently adjusted kinetic rate constants.

It can be concluded that even in using large grid, the accurate flow behavior is simulated by adopting the non-equilibrium state calculations with appropriate kinetic rate constants.

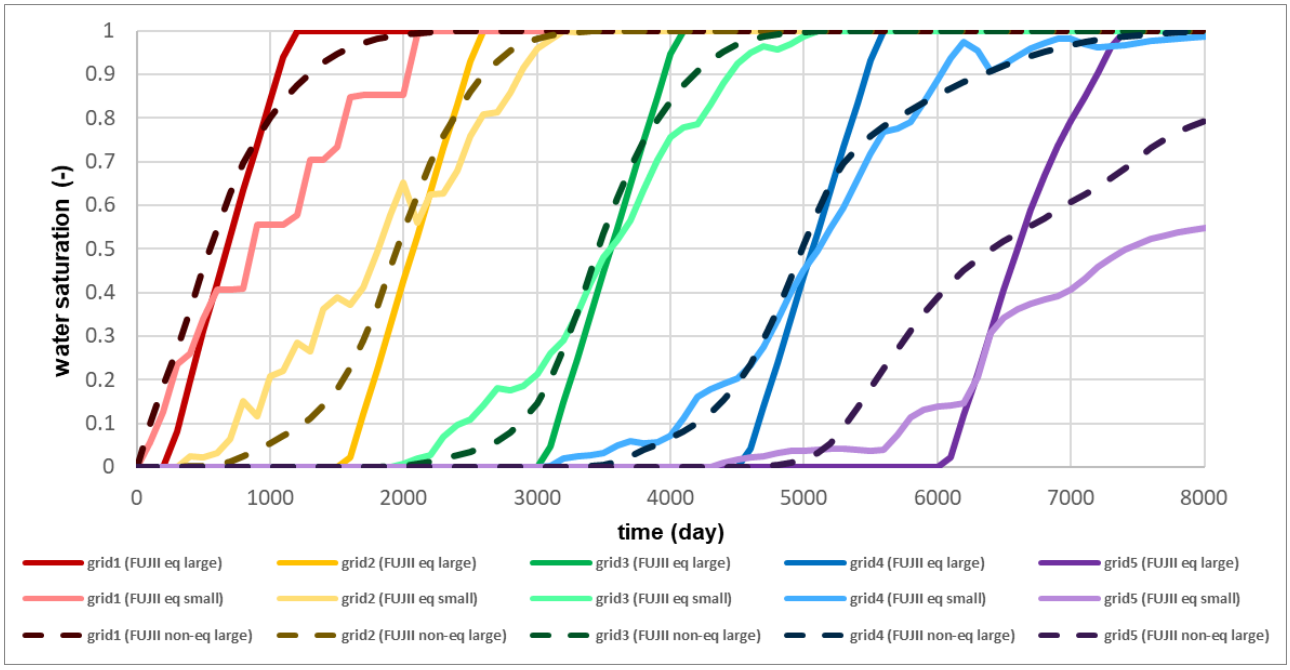

Figure 16: Time vs. Water saturation

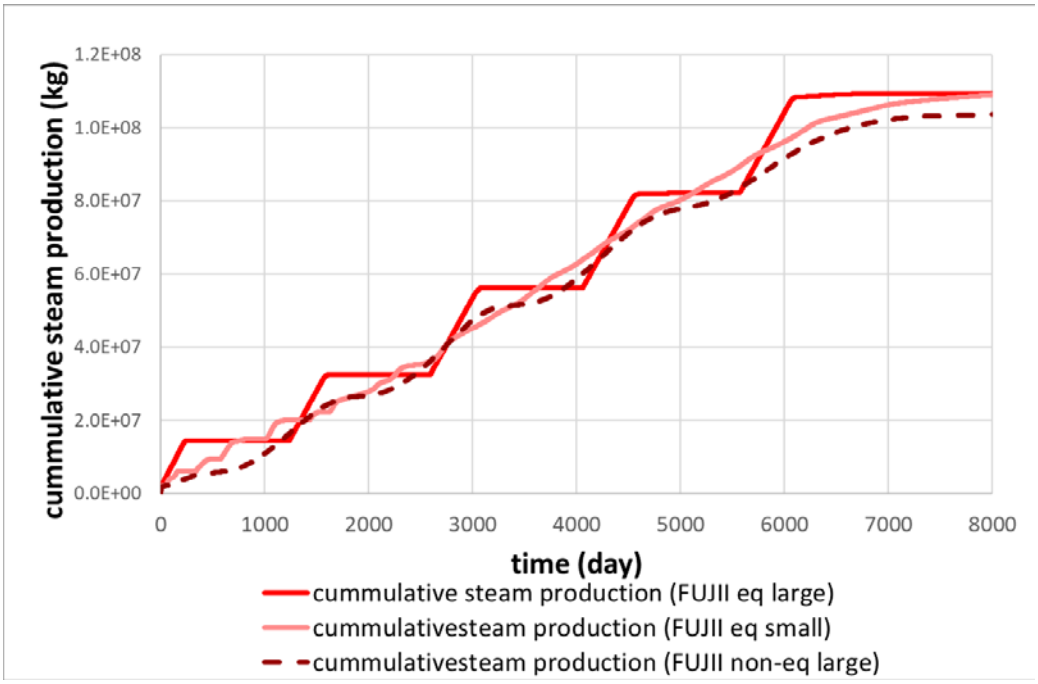

Figure 17: Cumulative steam production

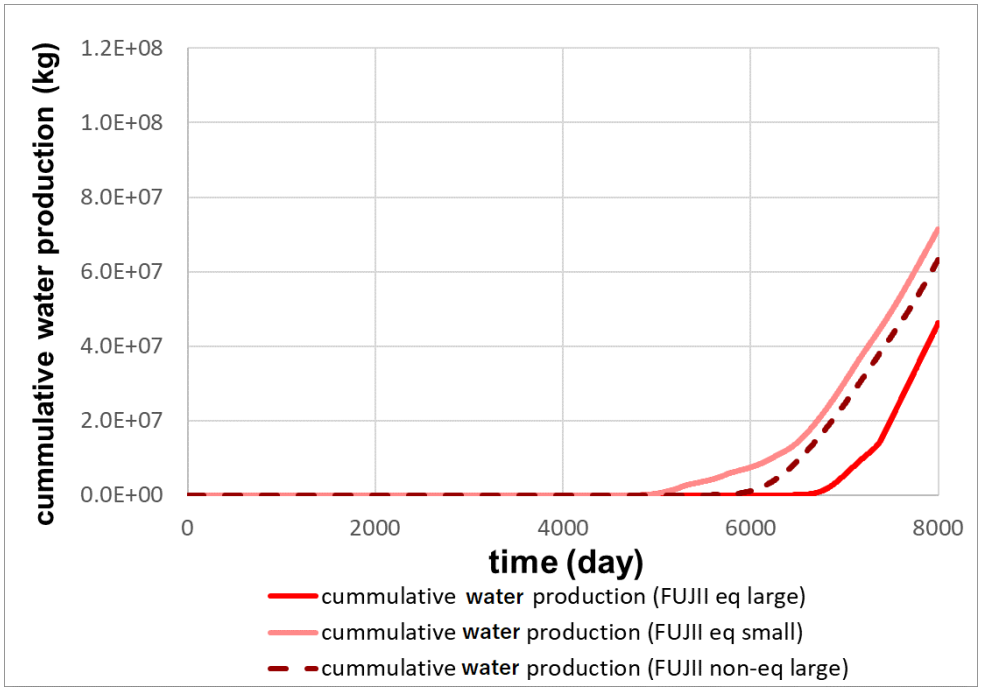

Figure 18: Cumulative water production

4. Reservoir Simulator (Fractured Model)

Since many fractures exist in geothermal reservoirs and these fractures are expected to be the main paths of fluid flow, it is essential to deal with fractures in geothermal reservoir simulation. In this research, we incorporated the function of double porosity models of Kazemi and MINC, which are popularly used in geothermal reservoir simulation, into the simulator developed in the previous chapters.

4.1 Double Porosity/Permeability Model

The double porosity model was developed by Kazemi in 1969. In the double porosity model, we assume the presence of fractures and matrices in each grid. Grids are supposed to be divided by sugar cubic model like Figure 19. The parts of slit stand for fractures, while the parts of the shape like sugar indicate matrices. Matrix is mainly composed of low permeability rock grains. On the other hand, fracture means the clack in the rock and its permeability is high.

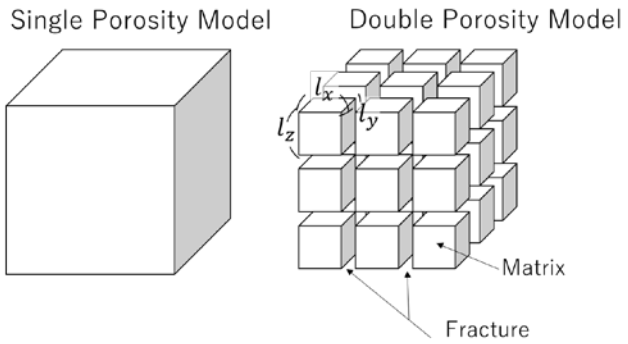

Figure 19: Sugar cubic model - idealized double porosity model of fractured porous media

Fluid flow in this model is schematically explained in Figure 24. In the double porosity system, the convection between fracture and adjacent fracture and the convection between matrix and fracture are only assumed. In dual permeability system, the convection between matrix and adjacent matrix is additionally assumed.

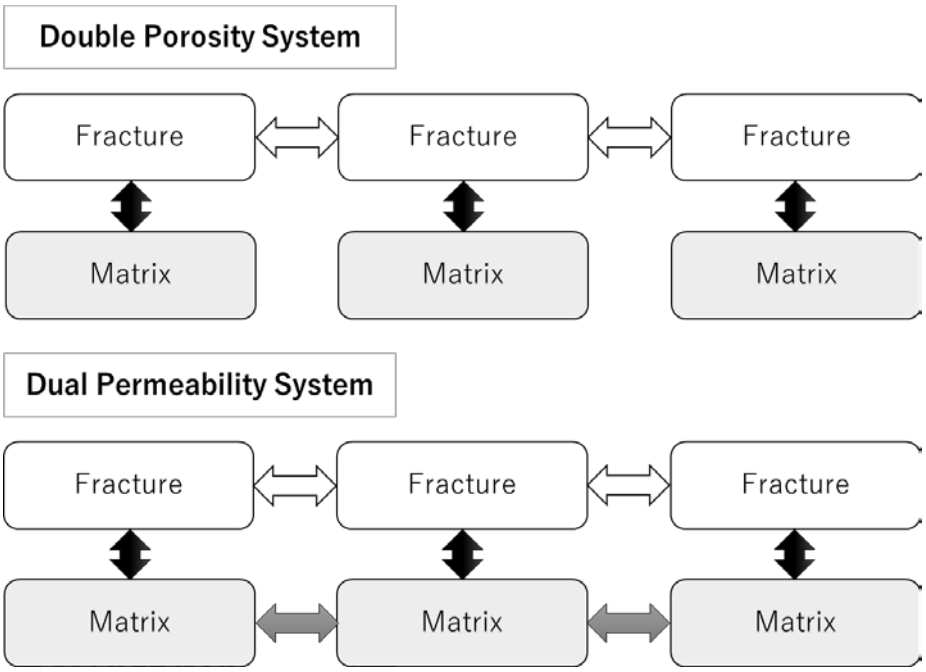

Figure 20: The flow system of double porosity model

The convection between matrix and fracture is calculated by the equation below.

$$[M \rightarrow F \ water \ convection] = 4k_m \left(\frac{k_{rw}\rho_w}{\mu_w} \right)_{up} \left\{ \frac{1}{l_x^{\,2}} + \frac{1}{l_y^{\,2}} + \frac{1}{l_z^{\,2}} \right\} \left(P_m - P_f \right) \tag{6}$$

, where l_x, l_y and l_z are called “fracture spacing”, which means the fracture interval in each direction as shown in Figure 19.

The governing equations of the simulator incorporating both the non-equilibrium fluid flow and the double porosity model (Kazemi) are given bellow. In this simulator, it is assumed that all the fractures are simple spaces and contain no rock grain parts within them. Therefore, the accumulation term in the fracture’s energy balance equation does not consider the internal energy of rocks.

(1) Equations of mass and energy balance at fracture

$$\vec{\nabla}\cdot\left(k_f\frac{k_{rwf}\rho_{wf}}{\mu_{wf}}(\vec{\nabla}P_f-\overline{\rho}_w g\vec{\nabla}D)\right)+4k_m\left(\frac{k_{rw}\rho_w}{\mu_w}\right)_{up}\left\{\frac{1}{l_x^{\,2}}+\frac{1}{l_y^{\,2}}+\frac{1}{l_z^{\,2}}\right\}\left(P_m-P_f\right)$$
$$+n_{wf}-n_{sf}+\tilde{q}_{w\_in}\rho_{w\_in}+\tilde{q}_{w\_out}\rho_{w\_out}=\frac{\partial}{\partial t}\left(\phi_f' S_{wf}\rho_{wf}\right) \tag{7}$$

$$\vec{\nabla}\cdot\left(k\frac{k_{rs}\rho_s}{\mu_s}(\vec{\nabla}P_f-\overline{\rho}_s g\vec{\nabla}D)\right)+4k_m\left(\frac{k_{rs}\rho_s}{\mu_s}\right)_{up}\left\{\frac{1}{l_x^{\,2}}+\frac{1}{l_y^{\,2}}+\frac{1}{l_z^{\,2}}\right\}\left(P_m-P_f\right)$$
$$-n_{wf}+n_{sf}+\tilde{q}_{s\_in}\rho_{s\_in}+\tilde{q}_{s\_out}\rho_{s\_out}=\frac{\partial}{\partial t}\left(\phi_f' S_{sf}\rho_{sf}\right) \tag{8}$$

$$\vec{\nabla}\cdot\left(k_f\frac{k_{rwf}\rho_{wf}H_w}{\mu_{wf}}(\vec{\nabla}P_f-\overline{\rho}_w g\vec{\nabla}D)\right)+\vec{\nabla}\cdot\left(k\frac{k_{rs}\rho_s H_s}{\mu_s}(\vec{\nabla}P_f-\overline{\rho}_s g\vec{\nabla}D)\right)$$
$$+4k_m\left(\frac{k_{rw}\rho_w H_w}{\mu_w}\right)_{up}\left\{\frac{1}{l_x^{\,2}}+\frac{1}{l_y^{\,2}}+\frac{1}{l_z^{\,2}}\right\}\left(P_m-P_f\right)+4k_m\left(\frac{k_{rs}\rho_s H_s}{\mu_s}\right)_{up}\left\{\frac{1}{l_x^{\,2}}+\frac{1}{l_y^{\,2}}+\frac{1}{l_z^{\,2}}\right\}\left(P_m-P_f\right)$$
$$+\vec{\nabla}\cdot\left(\lambda_{all}\vec{\nabla}\cdot T\right)+\tilde{q}_{w\_in}\rho_{w\_in}H_{w\_in}+\tilde{q}_{s\_in}\rho_{s\_in}H_{s\_in}+\tilde{q}_{w\_out}\rho_{w\_out}H_{w\_out}+\tilde{q}_{s\_out}\rho_{s\_out}H_{s\_out}$$
$$=\frac{\partial}{\partial t}\left(\phi_f' S_{wf}\rho_{wf}U_{wf}+\phi_f' S_{sf}\rho_{sf}U_{sf}\right) \tag{9}$$

(2) Equations of mass and energy balance at matrix

$$\vec{\nabla}\cdot\left(k_m\frac{k_{rwm}\rho_{wm}}{\mu_{wm}}(\vec{\nabla}P_m-\overline{\rho}_w g\vec{\nabla}D)\right)+4k_m\left(\frac{k_{rw}\rho_w}{\mu_w}\right)_{up}\left\{\frac{1}{l_x^{\,2}}+\frac{1}{l_y^{\,2}}+\frac{1}{l_z^{\,2}}\right\}\left(P_m-P_f\right)$$
$$+n_{wm}-n_{sm}=\frac{\partial}{\partial t}\left((1-\phi_f')\phi_m S_{wm}\rho_{wm}\right) \tag{10}$$

$$\vec{\nabla}\cdot\left(k\frac{k_{rsm}\rho_{sm}}{\mu_{sm}}(\vec{\nabla}P_m-\overline{\rho}_s g\vec{\nabla}D)\right)+4k_m\left(\frac{k_{rs}\rho_s}{\mu_s}\right)_{up}\left\{\frac{1}{l_x^{\,2}}+\frac{1}{l_y^{\,2}}+\frac{1}{l_z^{\,2}}\right\}\left(P_m-P_f\right)$$
$$-n_{wm}+n_{sm}=\frac{\partial}{\partial t}\left((1-\phi_f')\phi_m S_{sm}\rho_{sm}\right) \tag{11}$$

$$\vec{\nabla}\cdot\left(k_m\frac{k_{rwm}\rho_{wm}H_w}{\mu_{wm}}(\vec{\nabla}P_m-\overline{\rho}_w g\vec{\nabla}D)\right)+\vec{\nabla}\cdot\left(k\frac{k_{rsm}\rho_{sm}H_s}{\mu_{sm}}(\vec{\nabla}P_m-\overline{\rho}_s g\vec{\nabla}D)\right)$$
$$-4k_m\left(\frac{k_{rw}\rho_w H_w}{\mu_w}\right)_{up}\left\{\frac{1}{l_x^{\,2}}+\frac{1}{l_y^{\,2}}+\frac{1}{l_z^{\,2}}\right\}\left(P_m-P_f\right)-4k_m\left(\frac{k_{rs}\rho_s H_s}{\mu_s}\right)_{up}\left\{\frac{1}{l_x^{\,2}}+\frac{1}{l_y^{\,2}}+\frac{1}{l_z^{\,2}}\right\}\left(P_m-P_f\right)$$
$$+\vec{\nabla}\cdot\left(\lambda_{all}\vec{\nabla}\cdot T\right)$$
$$=\frac{\partial}{\partial t}\left((1-\phi_f')\phi_m S_{wm}\rho_{wm}U_{wm}+(1-\phi_f')\phi_m S_{sm}\rho_{sm}U_{sm}+(1-\phi_f')(1-\phi_m)\rho_r R_{capa}T_m\right) \tag{12}$$

, where ϕ_f' denotes the volume fraction of fracture [-], and ϕ_m is the porosity in matrix [-]. Note that the subscripts “f” and “m” stand for the fracture and matrix, respectively.

4.2 MINC Model

The Multiple Interacting Continua (MINC) model is developed by Pruess and Narasiham in 1982. As shown in Figure 22, MINC model is one of double porosity models, but the matrix part is discretized into a sequence of nested sub-grids. The MINC number of 4 means that “fracture” and “matrices 1-3” exist in each grid.

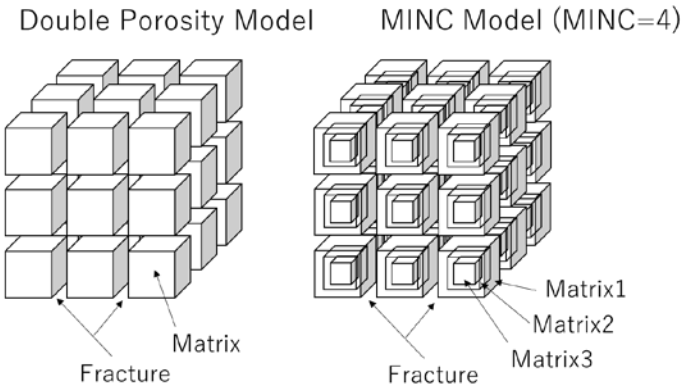

Figure 21: Idealized MINC model of fractured porous media

In the MINC model, we can more accurately describe the heat transfer in the matrix. In the double porosity model (Kazemi), the temperature of the entire parts of matrix is considered to be the same, while in the MINC model, we can calculate the different temperature for each part of the matrix. Therefore, we can express the temperature gradient in matrix by using MINC model, which results in the more accurate prediction for fluid flow.

As depicted bellow, in the MINC model, the convection between matrix and neighboring matrix is not considered.

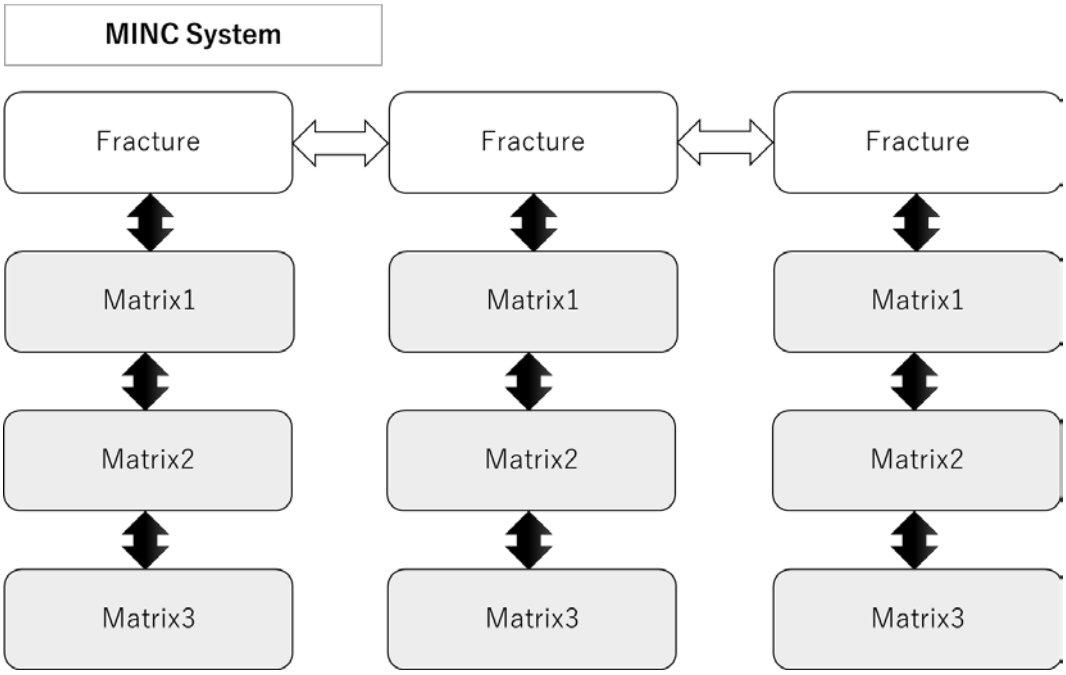

Figure 22: The flow system of MINC model

For simplicity, fracture is called “mesh(1)” and multiple sub-matrices are called “mesh(2,3,…,n)”. The convection between mesh(p) and mesh(p+1) within the same grid is calculated by applying the nodal distance from mesh(p) and mesh(p+1) to Darcy’s law as indicated in Figure 27 and Equation (13).

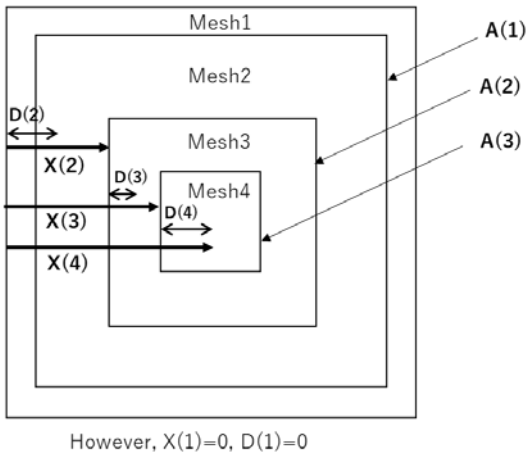

Figure 23: Schema of MINC model for one grid

$$[mesh(p+1) \rightarrow mesh(p)\ water\ convection] = k'_m \left(\frac{k_{rw}\rho_w}{\mu_w} \right)_{up} A_p \frac{1}{(D_p + D_{p+1}) l_x l_y l_z} \left(P_{p+1} - P_p \right) \tag{13}$$

, where A_p means the connecting surface between mesh(p) and mesh(p+1), and (D_p+D_{p+1}) means the nodal distance between mesh(p) and mesh(p+1).

D_p can be derived from equation below.

$$D_p = \left\{ X_p - X_{p-1} \right\} / 2 \tag{14}$$

, where X_p denotes the distance from surface of mesh(1) to mesh(p). This parameter X_p depends on ϕ'(p), which is the volume fraction of mesh(p). Once ϕ'(p) is given by user of the simulator, X_p can be estimated by solving Equation (15).

$$\sum_{i=1}^{p} \phi'(i) = \frac{l_x l_y l_z - (l_x - 2X_p)(l_y - 2X_p)(l_z - 2X_p)}{l_x l_y l_z} \tag{15}$$

Finally, we can obtain A_p as

$$A_p = 2\left\{ (l_x - 2X_p)(l_y - 2X_p) + (l_y - 2X_p)(l_z - 2X_p) + (l_x - 2X_p)(l_z - 2X_p) \right\}. \tag{16}$$

The governing equations of the simulator incorporating both the non-equilibrium fluid flow and the double porosity model (MINC) are given bellow.

(1) Equations of mass and energy balance f mesh p (p = 1)

$$\begin{aligned} &\vec{\nabla} \cdot \left(k_p \frac{k_{rwp}\rho_{wp}}{\mu_{wp}} (\vec{\nabla} P_p - \overline{\rho}_w g \vec{\nabla} D) \right) + k'_m \left(\frac{k_{rw}\rho_w}{\mu_w} \right)_{up} A_p \frac{1}{(D_p + D_{p+1}) l_x l_y l_z} \left(P_{p+1} - P_p \right) \\ &+ n_{wp} - n_{sp} + \tilde{q}_{w\_in}\rho_{w\_in} + \tilde{q}_{w\_out}\rho_{w\_out} \\ &= \frac{\partial}{\partial t} \left(\phi'_p S_{wp} \rho_{wp} \right) \end{aligned} \tag{17}$$

$$\vec{\nabla}\cdot\left(k_p\frac{k_{rsp}\rho_{sp}}{\mu_{sp}}(\vec{\nabla}P_p-\overline{\rho}_s g\vec{\nabla}D)\right)+k'_m\left(\frac{k_{rs}\rho_s}{\mu_s}\right)_{up}A_p\frac{1}{(D_p+D_{p+1})l_x l_y l_z}\left(P_{p+1}-P_p\right)$$
$$-n_{wp}+n_{sp}+\tilde{q}_{s\_in}\rho_{s\_in}+\tilde{q}_{s\_out}\rho_{s\_out}=\frac{\partial}{\partial t}\left(\phi'_p S_{sp}\rho_{sp}\right) \tag{18}$$

$$\vec{\nabla}\cdot\left(k_p\frac{k_{rwp}\rho_{wp}H_{wp}}{\mu_{wp}}(\vec{\nabla}P_p-\overline{\rho}_w g\vec{\nabla}D)\right)+\vec{\nabla}\cdot\left(k_p\frac{k_{rsp}\rho_{sp}H_{sp}}{\mu_{sp}}(\vec{\nabla}P_p-\overline{\rho}_s g\vec{\nabla}D)\right)$$
$$+\vec{\nabla}\cdot\left(\lambda_{all}\vec{\nabla}\cdot T\right)+\tilde{q}_{w\_in}\rho_{w\_in}H_{w\_in}+\tilde{q}_{s\_in}\rho_{s\_in}H_{s\_in}+\tilde{q}_{w\_out}\rho_{w\_out}H_{w\_out}+\tilde{q}_{s\_out}\rho_{s\_out}H_{s\_out} \tag{19}$$
$$=\frac{\partial}{\partial t}\left(\phi'_p S_{wp}\rho_{wp}U_{wp}+\phi'_p S_{sp}\rho_{sp}U_{sp}\right)$$

(2) Equations of mass and energy balance at mesh p (p = 2, 3, …, n)

$$\vec{\nabla}\cdot\left(k_p\frac{k_{rwp}\rho_{wp}}{\mu_{wp}}(\vec{\nabla}P_p-\overline{\rho}_w g\vec{\nabla}D)\right)$$
$$+k'_m\left(\frac{k_{rw}\rho_w}{\mu_w}\right)_{up}A_p\frac{1}{(D_p+D_{p+1})l_x l_y l_z}\left(P_{p+1}-P_p\right)-k'_m\left(\frac{k_{rw}\rho_w}{\mu_w}\right)_{up}A_{p-1}\frac{1}{(D_{p-1}+D_p)l_x l_y l_z}\left(P_p-P_{p-1}\right) \tag{20}$$
$$-n_{wp}+n_{sp}$$
$$=\frac{\partial}{\partial t}\left(\phi'_p\phi_m S_{sp}\rho_{sp}\right)$$

$$\vec{\nabla}\cdot\left(k_p\frac{k_{rsp}\rho_{sp}}{\mu_{sp}}(\vec{\nabla}P_p-\overline{\rho}_w g\vec{\nabla}D)\right)$$
$$+k'_m\left(\frac{k_{rs}\rho_s}{\mu_s}\right)_{up}A_p\frac{1}{(D_p+D_{p+1})l_x l_y l_z}\left(P_{p+1}-P_p\right)-k'_m\left(\frac{k_{rs}\rho_s}{\mu_s}\right)_{up}A_{p-1}\frac{1}{(D_{p-1}+D_p)l_x l_y l_z}\left(P_p-P_{p-1}\right) \tag{21}$$
$$-n_{wp}+n_{sp}$$
$$=\frac{\partial}{\partial t}\left(\phi'_p\phi_m S_{wp}\rho_{wp}\right)$$

$$\vec{\nabla}\cdot\left(k_p\frac{k_{rwp}\rho_{wp}H_{wp}}{\mu_{wp}}(\vec{\nabla}P_p-\overline{\rho}_w g\vec{\nabla}D)\right)+\vec{\nabla}\cdot\left(k_p\frac{k_{rsp}\rho_{sp}H_{sp}}{\mu_{sp}}(\vec{\nabla}P_p-\overline{\rho}_w g\vec{\nabla}D)\right)+\vec{\nabla}\cdot\left(\lambda_{all}\vec{\nabla}\cdot T\right) \tag{22}$$
$$=\frac{\partial}{\partial t}\left(\phi'_p\phi_m S_{wp}\rho_{wp}U_{wp}+\phi'_p\phi_m S_{sp}\rho_{sp}U_{sp}+\phi'_p(1-\phi_m)\rho_r R_{capa}T_p\right)$$

5. Validation and Case Studies

We executed several simulation runs using the simulator thus coded by combining the calculation functions for non-equilibrium state and the double porosity/permeability models, in order to examine how our simulator works and how the non-equilibrium state affect the fluid flow in fractured system.

5.1 One-dimensional Model (Dual Permeability)

First, we validated our simulator for the one-dimensional dual permeability system through the following three cases.

Case1:"STARS"
The results calculated by STARS

Case2:"FUJII K=1E-5"
The results calculated by our simulator assuming the equilibrium state with K_{gen_s}=K_{gen_w}=1E-5 [1/s/K]

Case3:"FUJII K=1E-8"
The results calculated by our simulator assuming the non-equilibrium state with K_{gen_s}=K_{gen_w}=1E-8 [1/s/K]

Since STARS can deal with the equilibrium state only, the results of "FUJII K=1E-5" (case2) should be in a good agreement with those of "STARS" (case1). "FUJII K=1E-8" (case3) is expected to have different results from "FUJII K=1E-5" (case2) and "STARS" (case1) because it calculates reservoir performances in the non-equilibrium state.

5.1.1 Simulation Specifications (Dual Permeability)

The reservoir model used in this simulation had dimension of x=1000 [ft], y=100 [ft] and z=100 [ft] with 10*1*1 grid system. It was initially filled with steam of 1500 [psia] and 320 [K]. An injection well and a production well were located at grids (1,1,1) and (10,1,1), respectively. The injection rate was assumed to be 500 [ft^3/day] and the injection rate was 1300 [ft^3/day]. Injected fluid temperature is 130 [℃]. The other simulation specifications are shown in Table **2**.

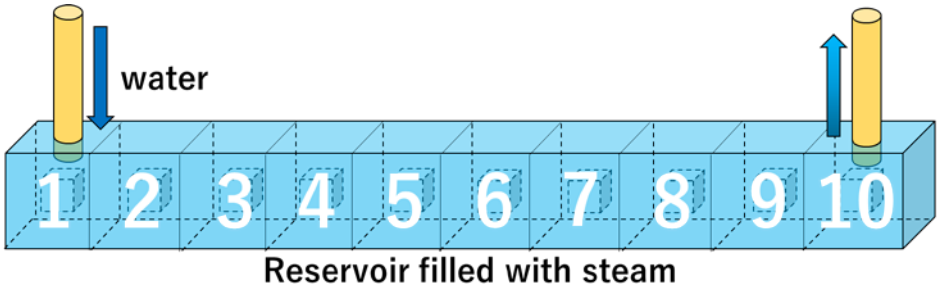

Figure 24: Reservoir model. Water is injected from grid 1 and fluid is produced from grid 10.

Table 2 **Simulation conditions**

Items	Description
Absolute effective permeability in fracture k_f [mD]	100
Absolute intrinsic permeability in matrix k'_m [mD]	0.0001
Fracture Volume fraction ϕ'_f [-]	0.1
Porosity in matrix at reference pressure ϕ_{m0} [-]	0.1
Compressibility of rock C_r [1/Pa]	1.4504×10^{-9}
Reference pressure P_{refp} [Pa]	101353.56
Rock heat capacity C_r [J/mol/K]	63.79
Density of rock ρ_r [mol/m^3]	38447.71
Time step [day]	1
Radius of injection well [inch]	6.0
Radius of production well [inch]	6.0
Fracture spacing x, y, z [ft]	10, 10, 10

5.1.2 Validation and Case Study (Dual Permeability)

First, we compared the results of “STARS” (case1) with those of ”FUJII K=1E-5” (case2).

The results of ”FUJII K=1E-5” (case2) fairly agreed with those of “STARS” (case1) as shown in Figure 25 through Figure 30. The water saturation profiles in fractures calculated in ”FUJII K=1E-5” (case2) were slightly different from those in “STARS” (case1), probably because the kinetic rate constant of 1E-5 [1/s/K] applied in case2 were slightly large to exactly express the equilibrium state in fractures, where fluid velocity is far faster than in matrices.

Since the difference in the simulation results between cases1 and 2 was sufficiently small, it was concluded that the double porosity model of our simulator functioned properly.

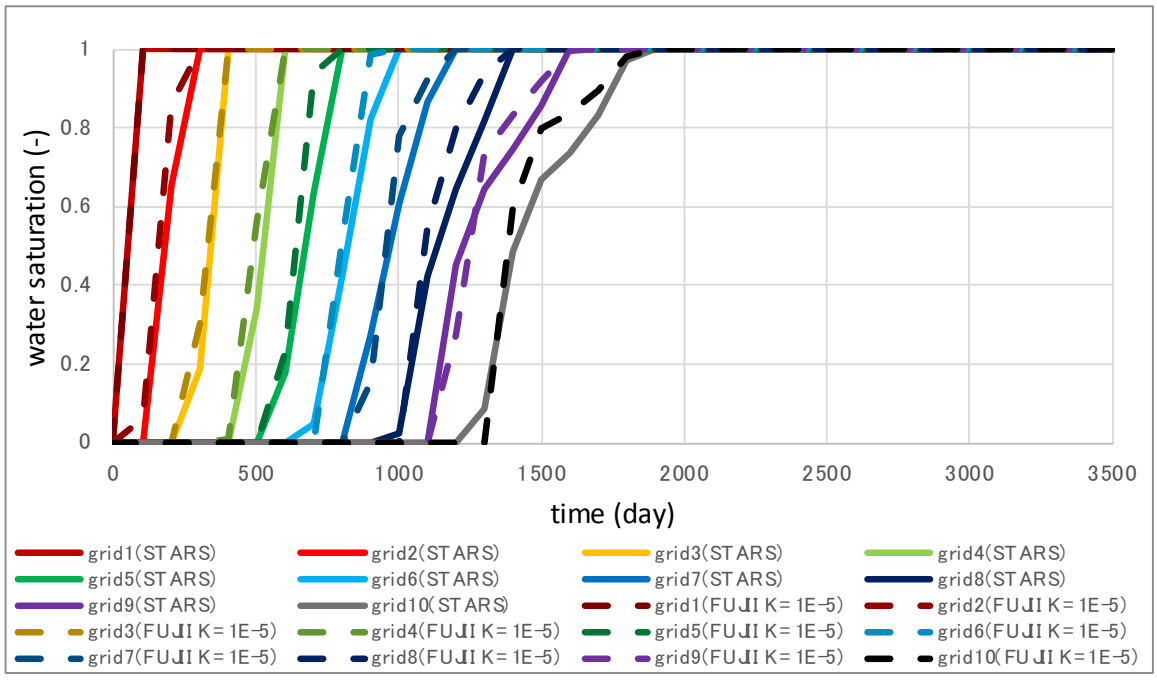

Figure 25: Time vs. Water saturation at fracture (“STARS”(case1): equilibrium, “FUJII K=1E-5”(case2): equilibrium).

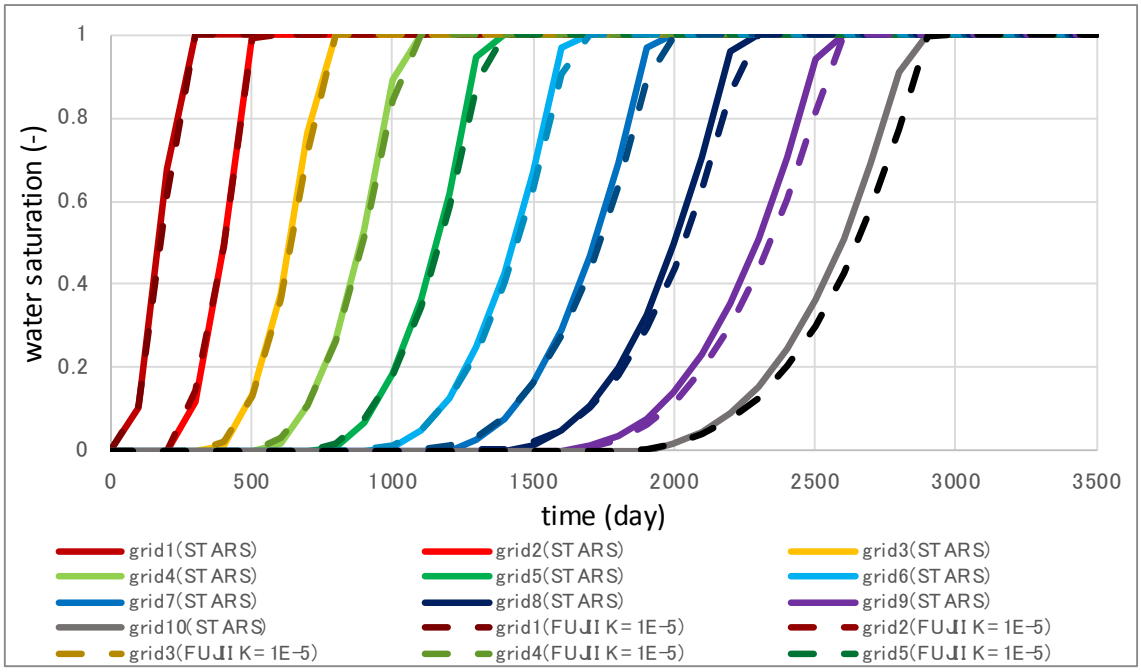

Figure 26: Time vs. Water saturation at matrix ("STARS"(case1): equilibrium, "FUJII K=1E-5"(case2): equilibrium).

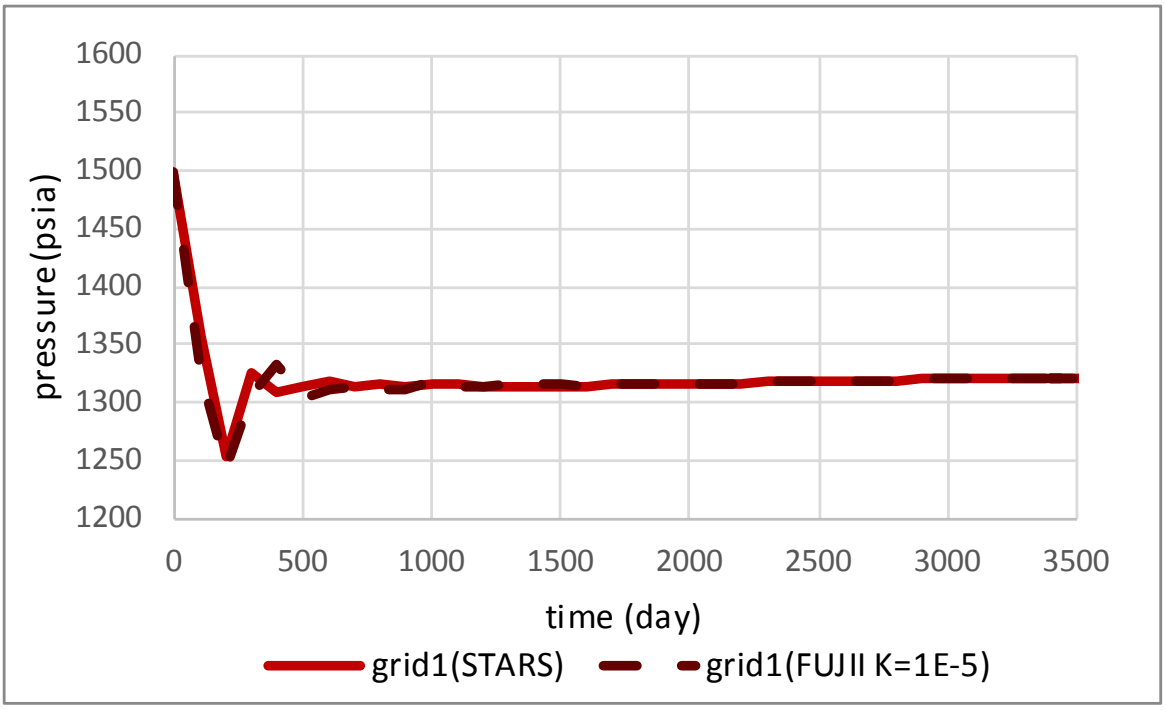

Figure 27: Time vs. Pressure at fracture ("STARS"(case1): equilibrium, "FUJII K=1E-5"(case2): equilibrium)..

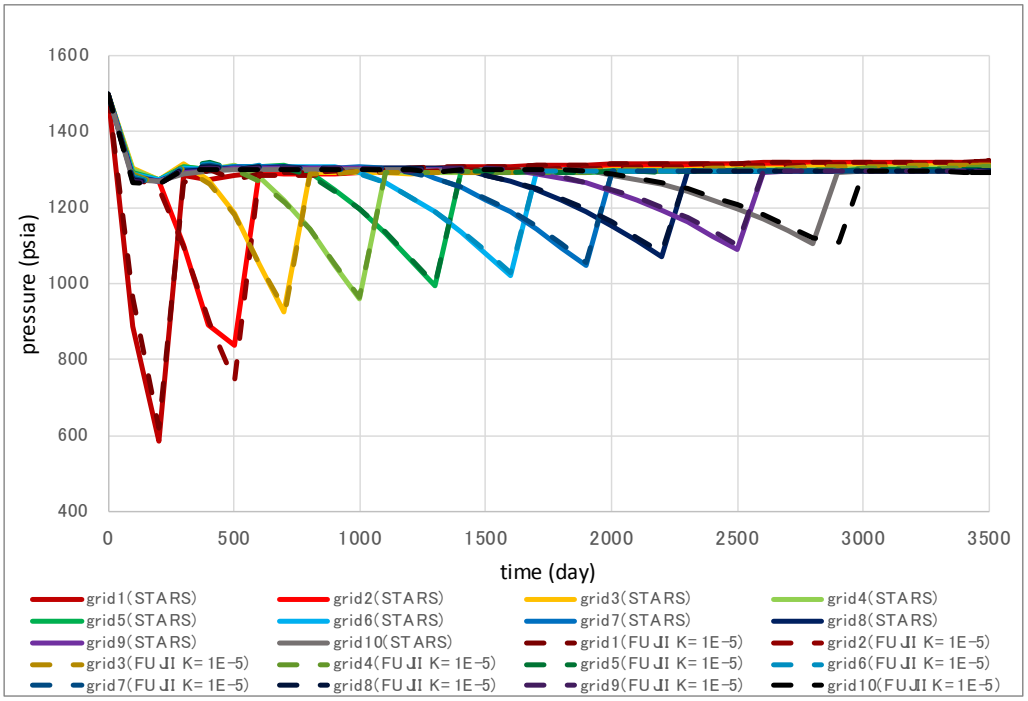

Figure 28: Time vs. Pressure at matrix ("STARS"(case1): equilibrium, "FUJII K=1E-5"(case2): equilibrium)..

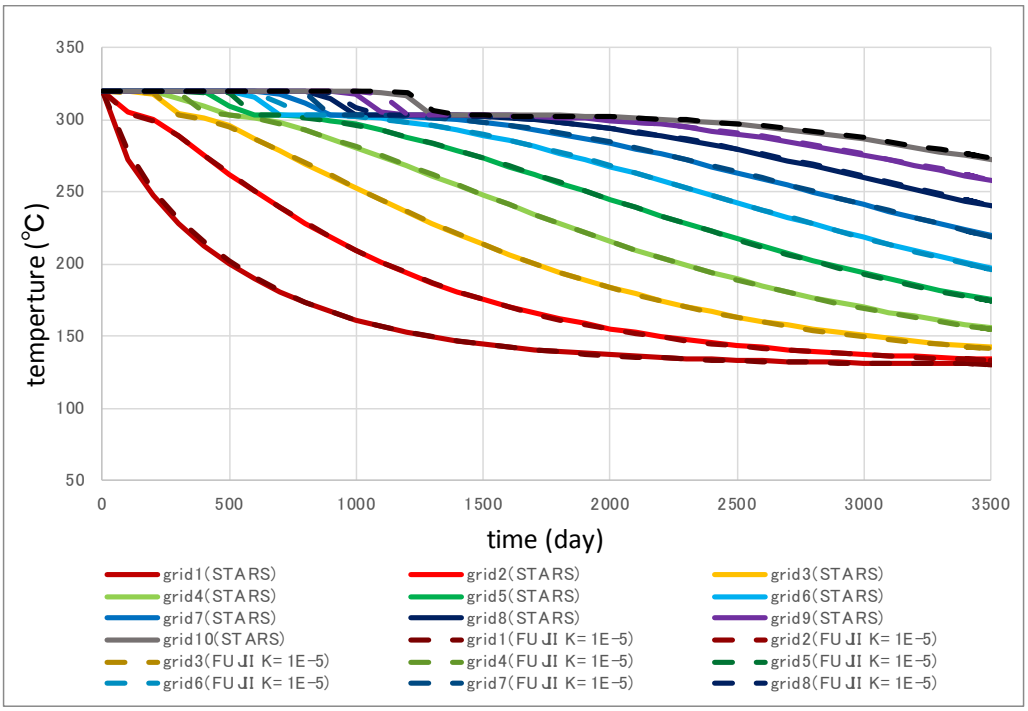

Figure 29: Time vs. Temperature at matrix ("STARS"(case1): equilibrium, "FUJII K=1E-5"(case2): equilibrium)..

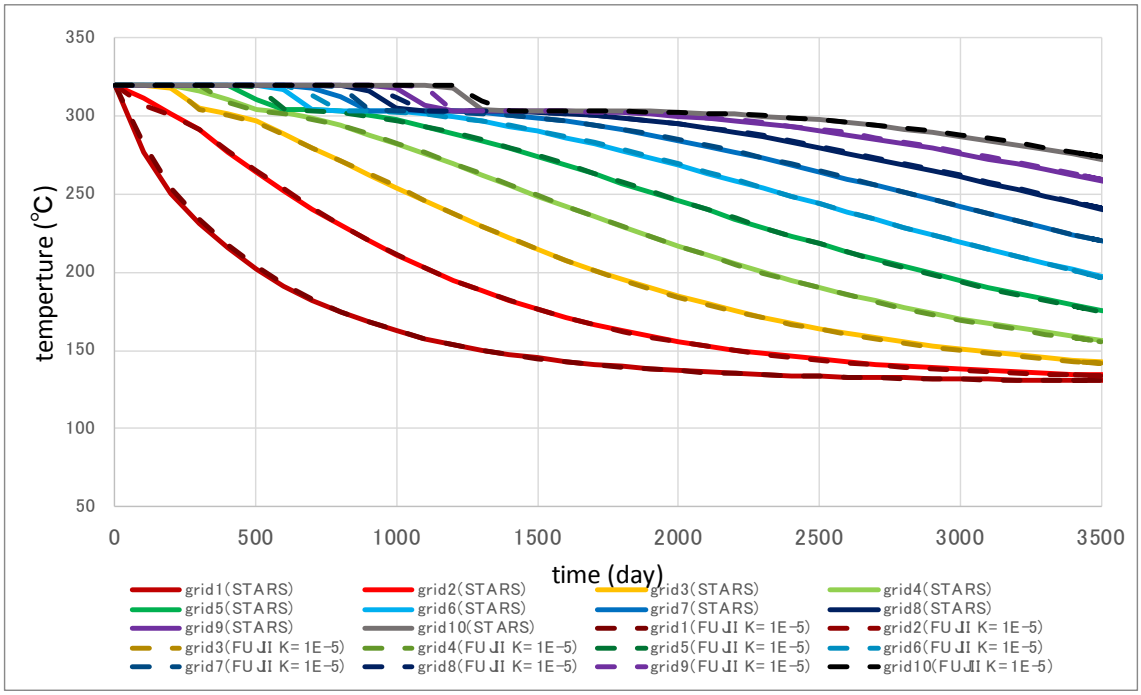

Figure 30: Time vs. Pressure at matrix ("STARS"(case1): equilibrium, "FUJII K=1E-5"(case2): equilibrium).

Next, we compared results of "STARS" (case1) with those of "FUJII K=1E-8" (case3).

As shown in Figure 31 through Figure 36, the results of "FUJII K=1E-8" (case3) were different from those of "STARS" (case1). Figure 31 shows that the water saturation in fractures started to increase earlier and reached 1 later in the non-equilibrium state, as in the single porosity system. On the other hand in matrices, the timings of both the start of increase in water saturation and the 100% of water saturation in case3 were slower than those in case1 as depicted in Figure 32.

In fractures, it takes a time for the injected water to be steam in the non-equilibrium state, which hastens the water breakthrough. In the later stage, even if the pressure-temperature condition becomes in the water region of the P-T diagram, the steam initially existing in fractures remains as steam for a longer time due to the non-equilibrium state, which results in the slow changes in water saturation in the non-equilibrium state.

On the other hand in matrices, since the quite small amount of water intrudes into matrices, water saturation increases due mainly to the condensation of steam, which should be slow in the non-equilibrium state. Hence, in the non-equilibrium state, the water saturation starts to increase and reach 1 more slowly than in the equilibrium state.

Since the fluid flow is dominant in fractures, the water breakthrough occurred earlier in the non-equilibrium state than in the equilibrium state, as shown in Figure 41.

Through the above simulation, we concluded that the function of our simulator for dealing with non-equilibrium state worked very well even with the double porosity/permeability model.

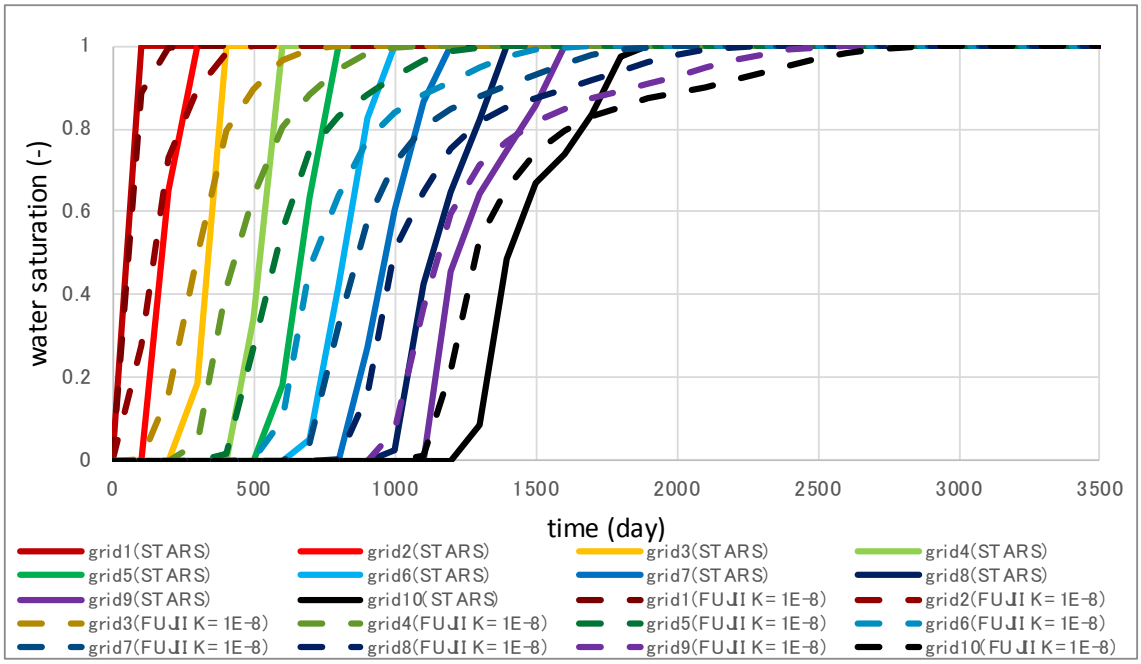

Figure 31: Time vs. Water saturation at fracture ("STARS"(case1): equilibrium, "FUJII K=1E-8"(case3): non-equilibrium).

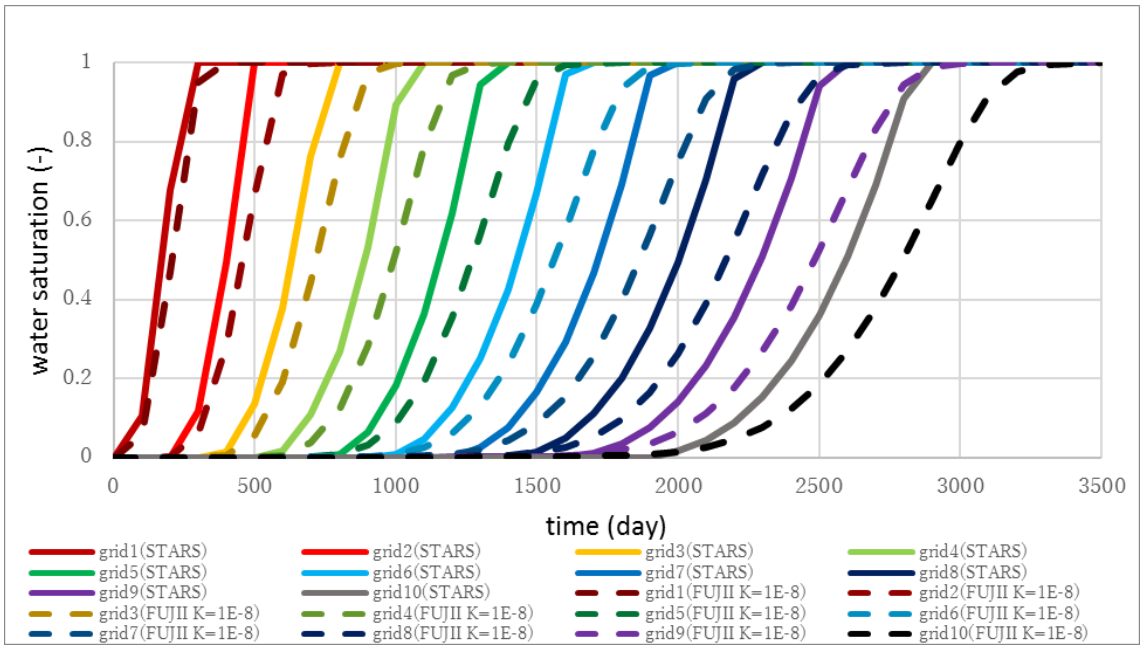

Figure 32: Time vs. Water saturation at matrix ("STARS"(case1): equilibrium, "FUJII K=1E-8"(case3): non-equilibrium).

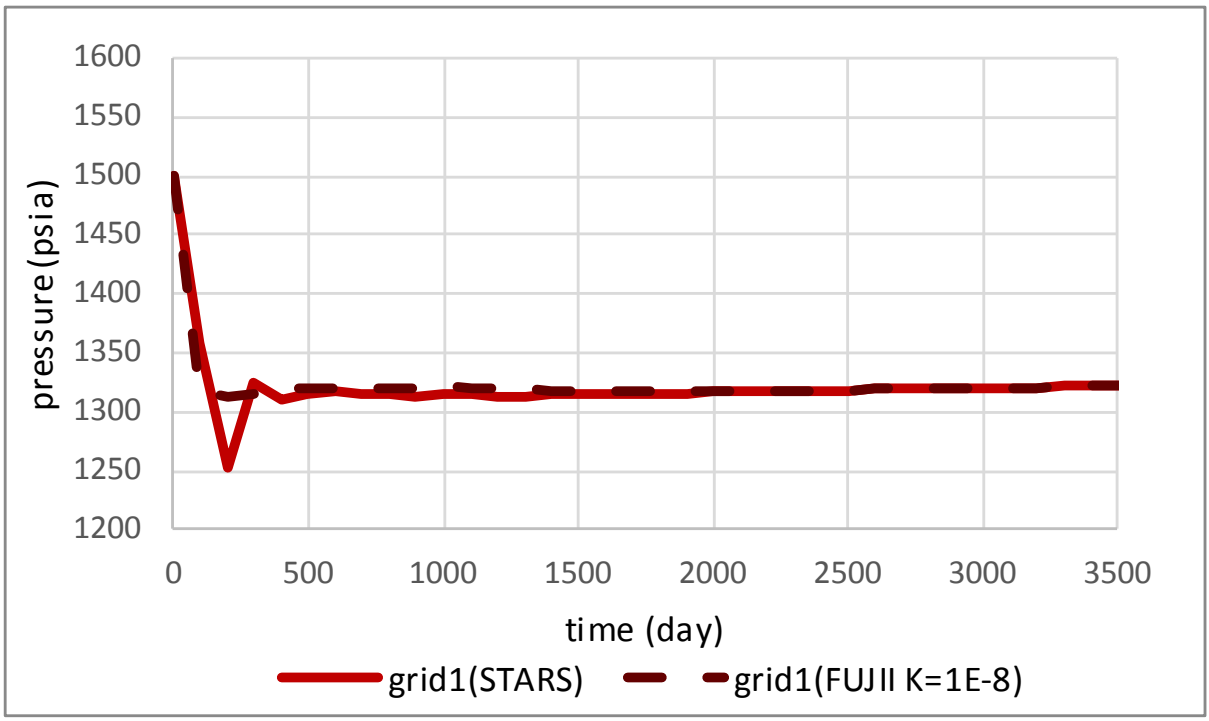

Figure 33: Time vs. pressure at fracture ("STARS"(case1): equilibrium, "FUJII K=1E-8"(case3): non-equilibrium).

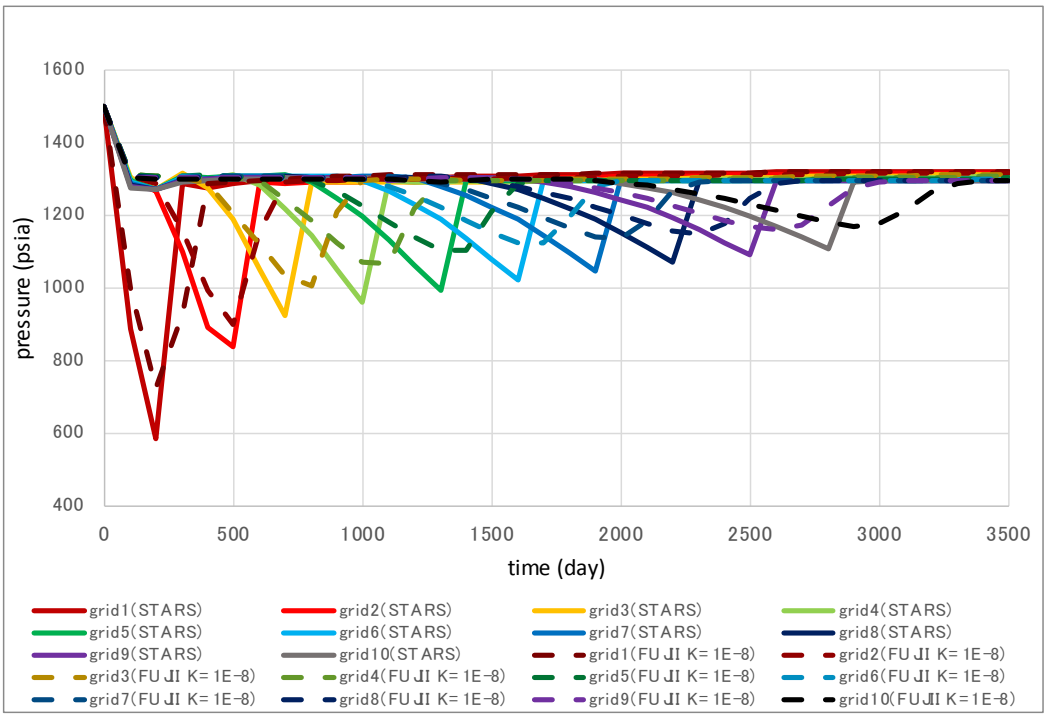

Figure 34: Time vs. pressure at matrix ("STARS"(case1): equilibrium, "FUJII K=1E-8"(case3): non-equilibrium).

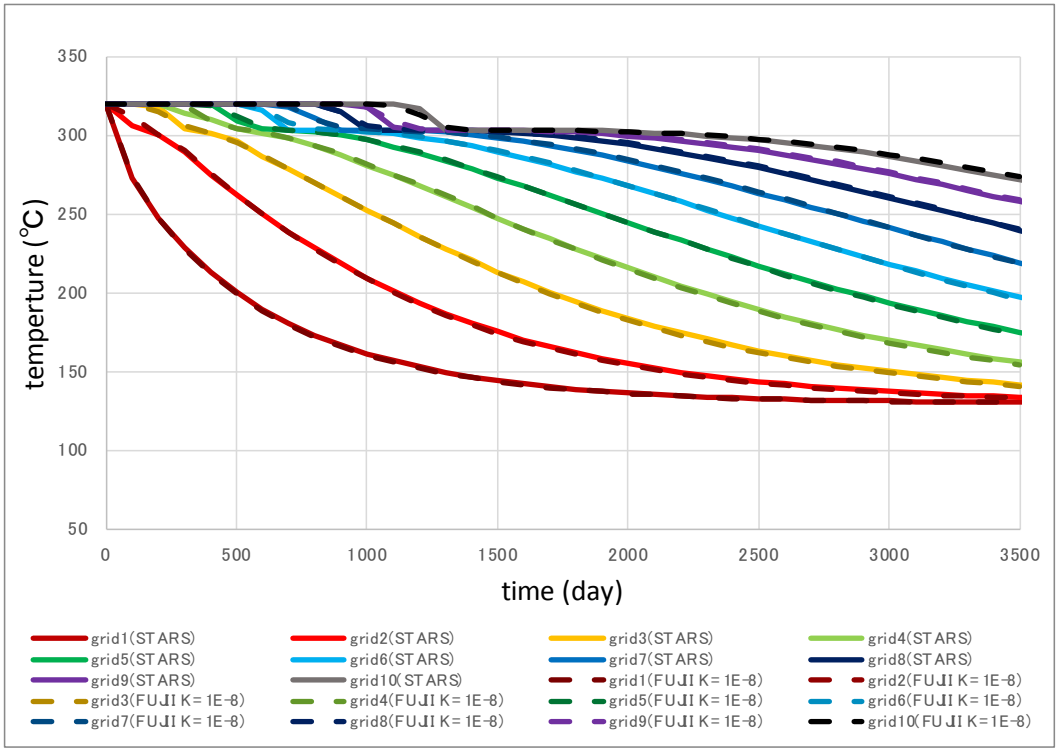

Figure 35: Time vs. temperature at fracture ("STARS"(case1): equilibrium, "FUJII K=1E-8"(case3): non-equilibrium).

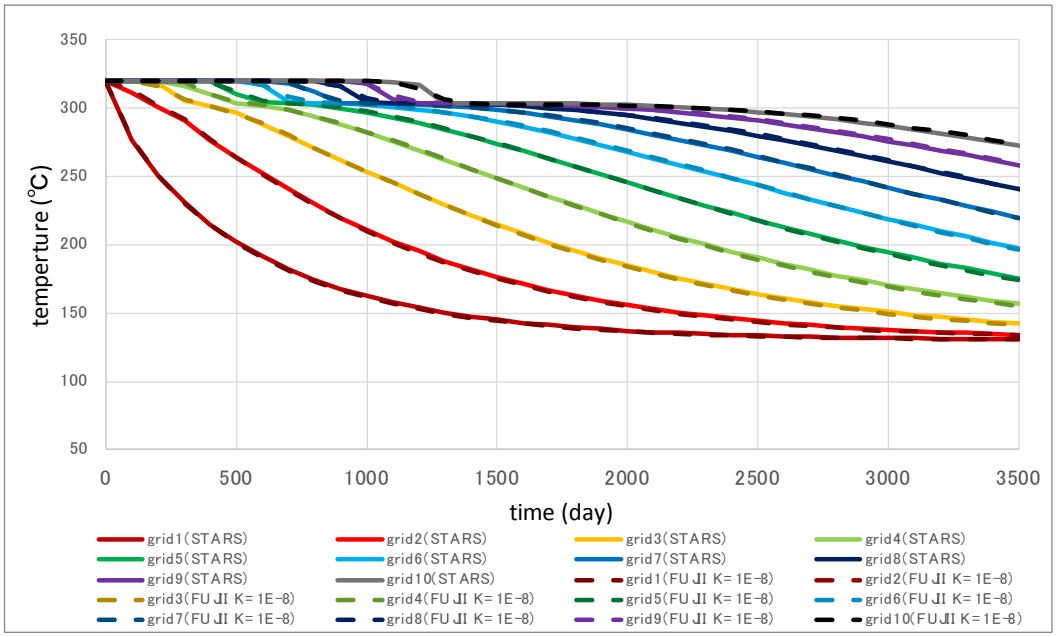

Figure 36: Time vs. temperature at matrix ("STARS"(case1): equilibrium, "FUJII K=1E-8"(case3): non-equilibrium).

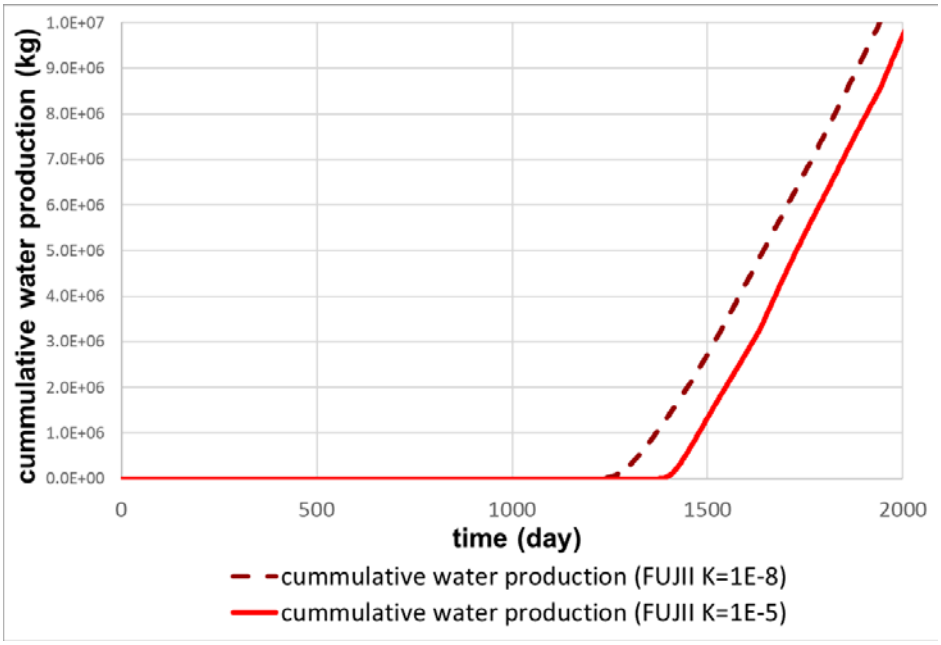

Figure 37: Cumulative water production ("FUJII K=1E-5"(case2): equilibrium, "FUJII K=1E-8"(case3):non-equilibrium).

5.2 Three-dimensional Model (Double Porosity)

In order to validate the double porosity model of our simulator in the three-dimensional system, we conducted simulation for the following these three cases.

Case1:"STARS"
The results calculated by STARS

Case2:"FUJII K=1E-5"
The results calculated by our simulator assuming the equilibrium state with $K_{gen\_s}=K_{gen\_w}$=1E-5 [1/s/K]

Case3:"FUJII K=1E-8"
The results calculated by our simulator assuming the non-equilibrium state with $K_{gen\_s}=K_{gen\_w}$=1E-8 [1/s/K]

5.2.1 Simulation Specifications (Double Porosity)

The reservoir model used in this simulation had dimensions of x=600 [ft], y=600 [ft] and z=600 [ft] with 3*3*3 grid system. It was initially filled with steam of 1500 [psia] and 325 [K]. An Injection well and a production well are located at grids (1,1,3) and (3,3,3), respectively. The injection rate was assumed to be 4000 [ft^3/day] and the bottom hole pressure of production well was assumed to be 1300 [psia]. Injected fluid temperature is 80 [℃]. The other simulation specifications are shown in Table **2**.

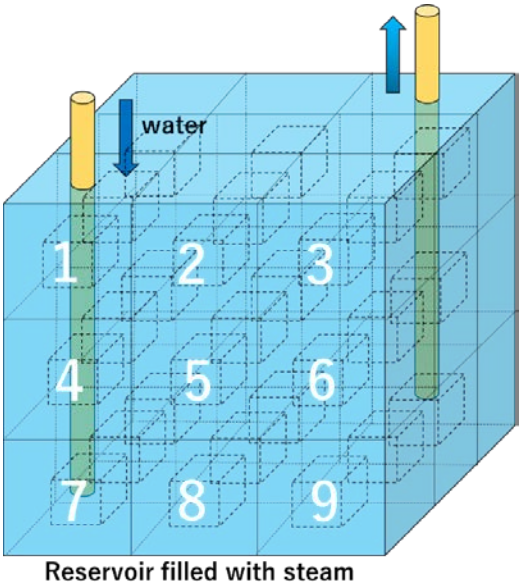

Figure 38: Reservoir model. Water is injected from grid 7 and fluid is produced from grid 27.

5.2.2 Validation and Case Study (Double Porosity)

First, we compared the results of two cases of simulation, “STARS” (case1) and “FUJII K=1E-5” (case2).

Since both of cases considered the equilibrium state, the results of “FUJII K=1E-5” (case2) showed a good agreement with those of “STARS” (case1) as shown in Figure 39 and Figure 40, which suggests that the double porosity model incorporated into our simulator functioned well in the three-dimensional system. Note that the slight difference in the results between these two cases should have been caused by the insufficiently small kinetic rate constant as in the one-dimensional system.

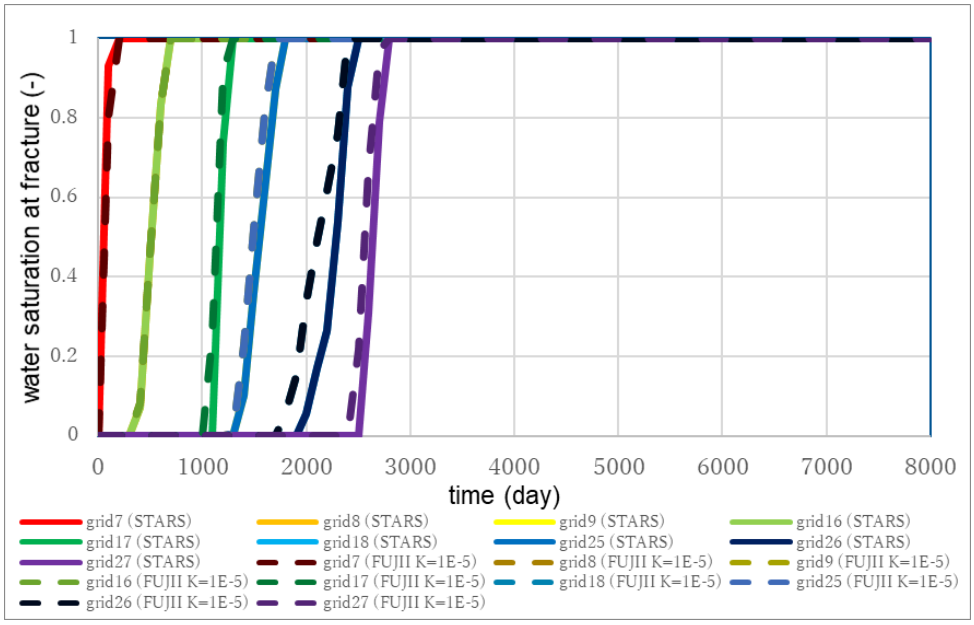

Figure 39: Time vs. water saturation at fracture (“STARS”(case1): equilibrium, “FUJII K=1E-5”(case2): non-equilibrium).

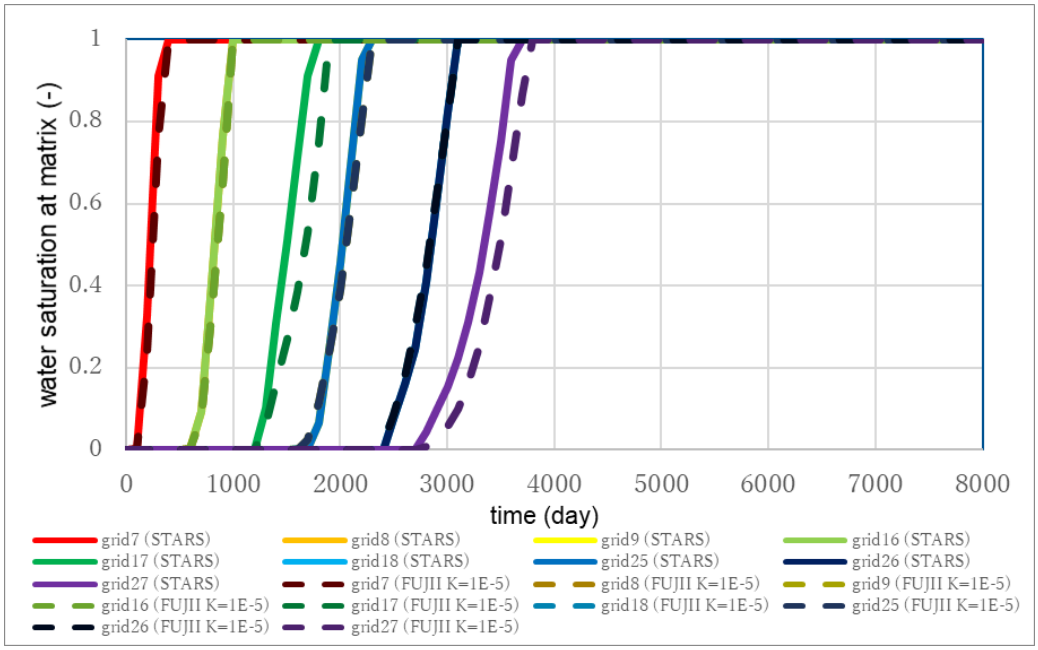

Figure 40: Time vs. water saturation at matrix ("STARS"(case1): equilibrium, "FUJII K=1E-5"(case2): equilibrium).

Next, we compared the two cases of simulation, "STARS" (case1) and "FUJII K=1E-8" (case3).

As shown in Figure 41 and Figure 42, it was confirmed that the results in the three-dimensional system showed the same tendencies as in the one-dimensional system. That is, in the non-equilibrium state, the water saturation in fractures started to increase earlier and reached 1 later than in the equilibrium state, while the timings of both the start of increase in water saturation and the 100% of water saturation were slower than in the equilibrium state.

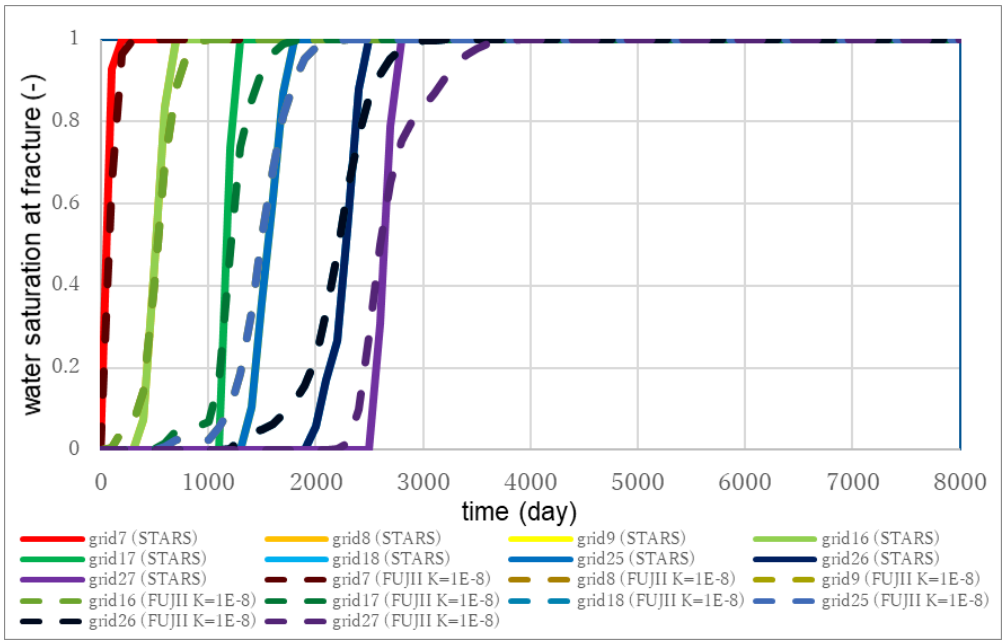

Figure 41: Time vs. water saturation at fracture ("STARS"(case1): equilibrium, "FUJII K=1E-8"(case3): non-equilibrium).

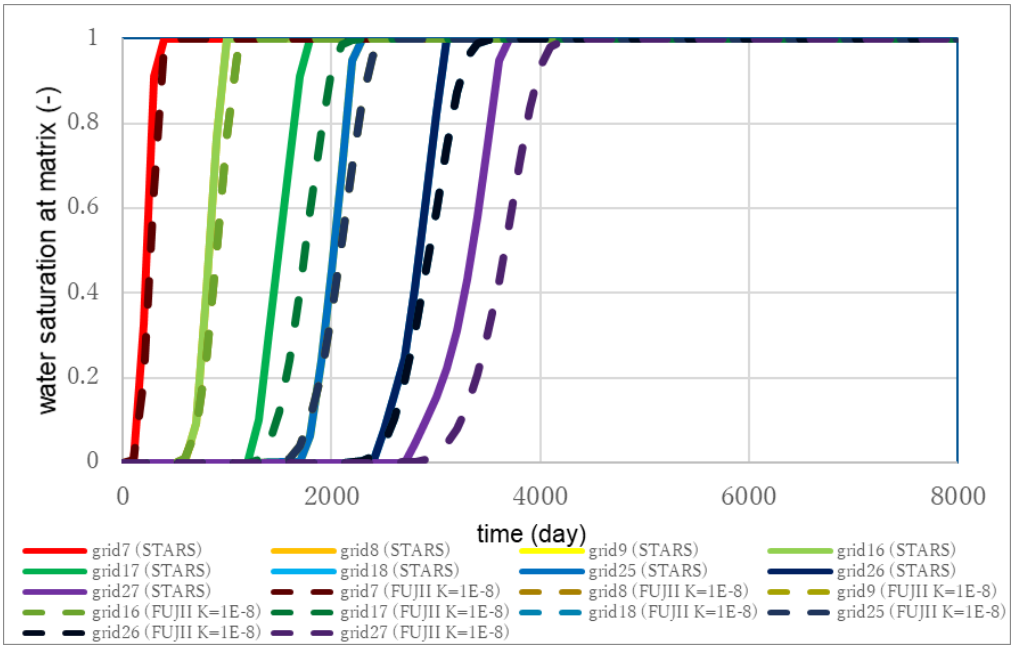

Figure 42: Time vs. water saturation at matrix ("STARS"(case1): equilibrium, "FUJII K=1E-8"(case3): non-equilibrium).

5.3 One-dimensional Model (MINC Model)

Since STARS are not equipped with the MINC model, we conducted the following four case studies for investigating the effects of the division of matrix, fracture spacing and overall thermal conductivity on the reservoir performances simulated with the MINC model, only using our simulator developed in this research. Note that the matrix part in each grid were divided into two (MINC3) or four (MINC5) sub-matrices in these case studies.

Case1:" FUJII MINC3[5] 10H"
The results calculated by our simulator with small fracture spacing (l_x= l_y=l_z=10 [ft]) and high thermal conductivity ($\lambda_{all\,m}$=328320 [J/m/day/K])

Case2:" FUJII MINC3[5] 10L"
The results calculated by our simulator with small fracture spacing (l_x= l_y=l_z=10 [ft]) and low thermal conductivity ($\lambda_{all\,m}$=103680 [J/m/day/K])

Case3:" FUJII MINC3[5] 100H"
The results calculated by our simulator with large fracture spacing (l_x= l_y=l_z=100 [ft]) and high thermal conductivity ($\lambda_{all\,m}$=328320 [J/m/day/K])

Case4:" FUJII MINC3[5] 100L"
The results calculated by our simulator with large fracture spacing (l_x= l_y=l_z=100 [ft]) and low thermal conductivity ($\lambda_{all\,m}$=103680 [J/m/day/K])

If the fracture spacing is large and/or the thermal conductivity is low, the temperature gradient in matrix should be large because fluid and heat are not interfered efficiently. Therefore, in these cases, it is expected that the simulation results should vary depending on the number of sub-matrices in the MINC model. On the other hand, if fracture spacing is

small enough and thermal conductivity is high enough, the temperature gradient in matrix should be small because of the good communication of fluid and heat, which should result in the small effect of the number of sub-matrices in the MINC model on simulation results.

5.3.1 Simulation Specifications (MINC Model)

As shown in Figure 43, the reservoir model used in this simulation had dimensions of x=1000 [ft], y=100 [ft] and z=100 [ft] with 10*1*1 grid system. It was initially filled with steam of 1500 [psia] and 320 [K]. An Injection well and a production well were located at grids (1,1,1) and (10,1,1), respectively. The injection rate was assumed to be 800 [ft^3/day] and the injection rate was 1500 [ft^3/day].

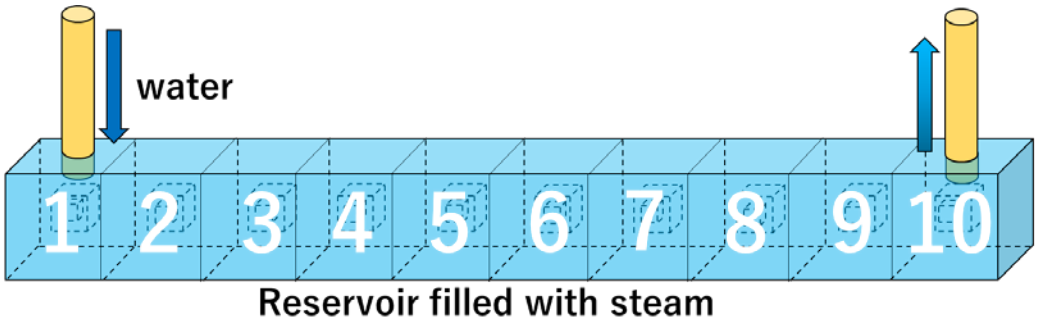

Figure 43: Reservoir model. Water is injected from grid 1 and fluid is produced from grid 10.

5.3.2 Case Study (MINC Model)

Figure 44 through Figure 47 show the change in water saturation in fractures. As shown in Figure 44 and Figure 45, in "FUJII MINC3[5] 10H" (case1) and "FUJII MINC3[5] 10L" (case2), which were the cases of small fracture spacing, no difference was observed in the simulation results between MINC3 (two sub-matrices) and MINC5 (four sub-matrices). On the other hand, as shown in Figure 46, in "FUJII MINC3[5] 100H" (case3), which was the case of large fracture spacing and high thermal conductivity, the water saturation profiles simulated with MINC5 was more like those in the non-equilibrium state (i.e., early start of increase in water saturation and slow increase in water saturation). This tendency was exaggerated as the thermal conductivity became lower, as shown in Figure 47.

Since our simulator with the MINC model calculated the reasonable reservoir performances, it can be concluded that the MINC model of our simulator functioned properly.

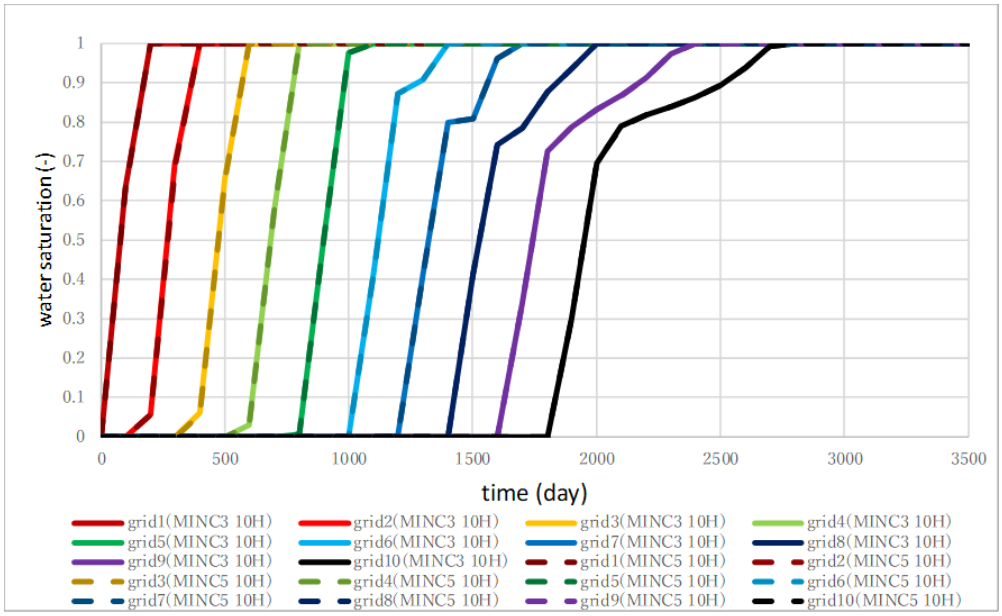

Figure 44: Time vs. water saturation in fracture (fracture spacing: small, thermal conductivity: high)

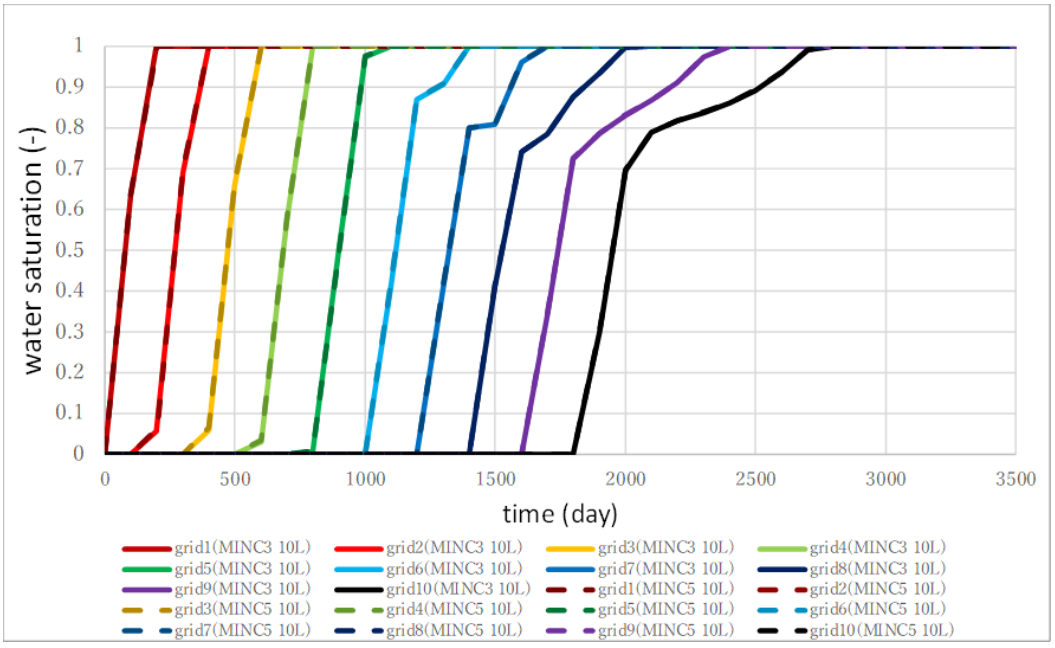

Figure 45: Time vs. water saturation in fracture (fracture spacing: small, thermal conductivity: low)

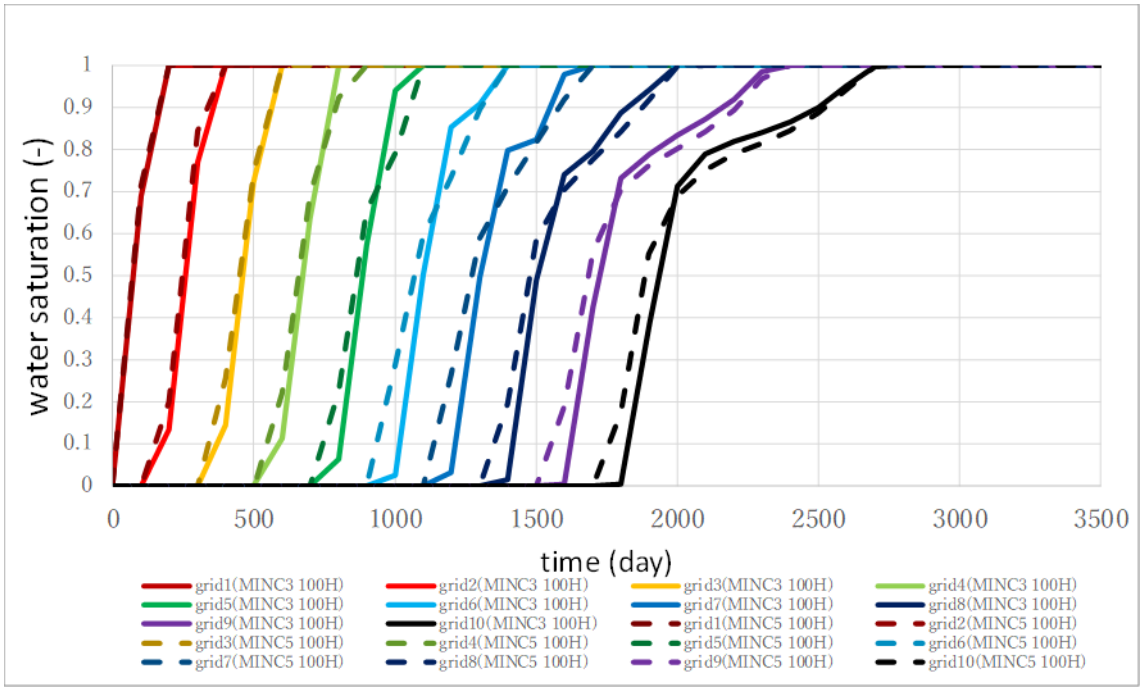

Figure 46: Time vs. water saturation in fracture (fracture spacing: large, thermal conductivity: high)

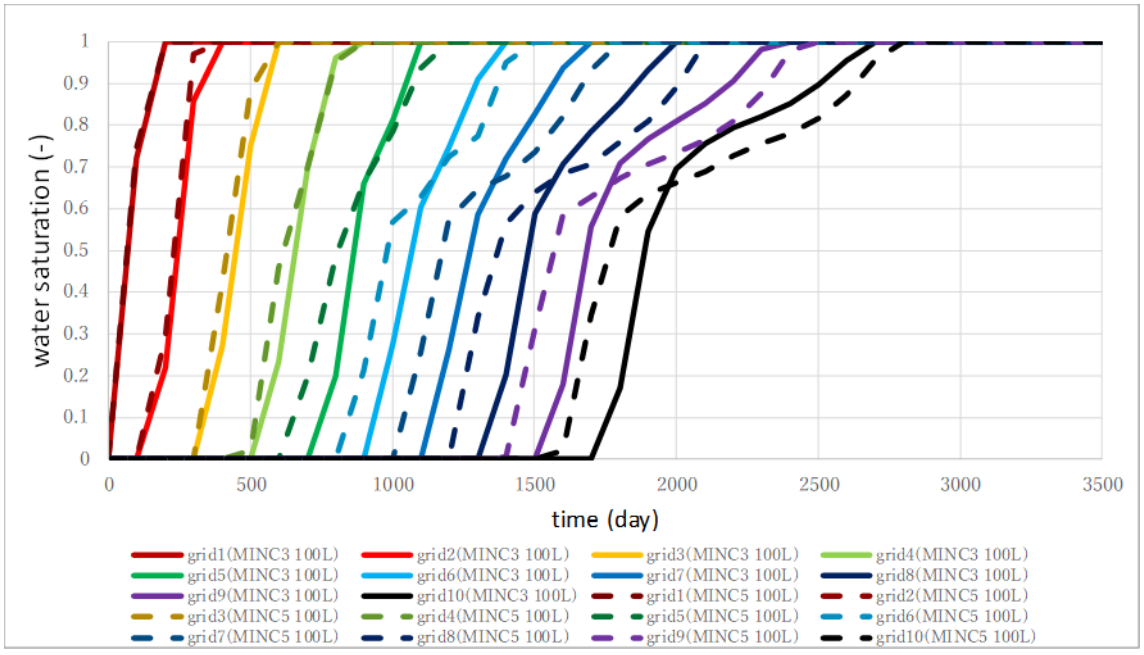

Figure 47: Time vs. water saturation in fracture (fracture spacing: large, thermal conductivity: low)

6. Conclusions

In this research, a new geothermal reservoir simulator which can deal with the non-equilibrium state and fractured system was successfully developed. Through the simulation using this simulator, the following conclusions were obtained.

(1) It was confirmed that our simulator worked accurately for the equilibrium state fluid flow through the comparison with the simulation results by STARS of CMG.

(2) Applying the small kinetic rate constants of $K_{gen\ \_w}$ and $K_{gen\ \_s}$ (approximately 1E-8 [1/s/K]), the non-equilibrium phase alteration could be reproduced in our simulator. In the non-equilibrium state, the water saturation was predicted to start to increase earlier and to increase more slowly than in the equilibrium state, which suggests that our simulator can predict the geothermal reservoir performances with artificial recharge more accurately.

(3) The results of the simulation assuming the equilibrium state with fine grids was close to those assuming the non-equilibrium state with coarse grids rather than to those assuming the equilibrium state with coarse grids. These results show the promise of the non-equilibrium flow simulation combining appropriate kinetic rate constants and coarse grid for more accurate simulation in shorter computational time.

(4) It was revealed that the non-equilibrium condition hastened the movement of the injected (recharge) water through fractures, which resulted in the water breakthrough earlier than predicted by conventional (equilibrium type) simulators.

REFERENCES

Computer Modeling Group, “STARS User’s Guide Version 2013”, (2013)

Heinemann Z. E. and Mittermeir G. M., “Derivation of the Kazemi–Gilman–Elsharkawy Generalized Dual Porosity Shape Factor”, TRANSPORT IN POROUS MEDIA, 91(1), pp.123-132., (2011)

Ishigami, Y., Sabawon, A. and Kurihara, M., “Development of Numerical Simulator for Predicting Non-Equilibrium Steam-water Flow Behavior and Its Application to Estimating Steam-water Relative Permeability”, Geothermal Resources Council Transactions, 41, pp.2008-2037, (2017)

Narasimhan, T. N. and Witherspoon, P. A., “Numerical Model for Saturated-Unsaturated Flow in Deformable Porous Media 1. Theory”, Water Resources Research, 13(3), pp.657-664, (1977)

Pruess, K., “GMINC - A MESH GENERATOR FOR FLOW SIMULATIONS IN FRACTURED RESERVOIRS”, Earth Science Division Lawrence Berkeley Laboratory, (1983)

Pruess, K. and Narasimhan, T. N., “A Practical Method for Modeling Fluid and Heat Flow in Fractured Porous Media”, SOCIETY OF PETROLEUM ENGINEERS JOURNAL, 25(1), pp.14-26, (1985)

Pruess, K., Oldenburg, C. and Moridis, G., “TOUGH2 USER’S GUIDE, VERSION 2.0”, (1999)